Distribution Agreement

In presenting this thesis or dissertation as a partial fulfillment of the requirements for an advanced degree from Emory University, I hereby grant to Emory University and its agents the non-exclusive license to archive, make accessible, and display my thesis or dissertation in whole or in part in all forms of media, now or hereafter known, including display on the world wide web. I understand that I may select some access restrictions as part of the online submission of this thesis or dissertation. I retain all ownership rightsto the copyright of the thesis or dissertation. I also retain the right to use in future works (such as articles or books) all or part of this thesis or dissertation.

Signature:

Andrei Zholud

Date

Effect of spin current on magnetization dynamics

by
Andrei Zholud
Doctor of Philosophy
Physics

Sergei Urazhdin, Ph.D
Advisor

Phillip First, Ph.D
Committee Member

Justin Burton, Ph.D
Committee Member

Khalid Salaita, Ph.D
Committee Member

Stefan Boettcher, Ph.D
Committee Member

Hayk Harutyunyan, Ph.D
Committee Member

Accepted:

Lisa A. Tedesco, Ph.D.
Dean of the James T. Laney School of Graduate Studies

Date

Effect of spin current on magnetization dynamics

by

Andrei Zholud
M.S., National Academy of Sciences of Belarus, 2010
B.S., Belarusian State University, 2009

Advisor: Sergei Urazhdin, Ph.D.

An abstract of
A dissertation submitted to the Faculty of the
James T. Laney School of Graduate Studies of Emory University
in partial fulfillment of the requirements for the degree of
Doctor of Philosophy
in Physics
2017

Abstract

The main subject of this work is the magnetization dynamics excited in magnetic nanostructures by spin polarized electrical or pure spin current. This research is important for the development of spintronic devices – devices that in addition to the electron charge exploit the spin degree of freedom for information storage, transmission, processing, and/or for sensing. The research presented in this thesis addresses three relevant problems: 1) Enhancing the efficiency of spin current-driven spintronic devices by optimizing their geometry; 2) Enhancing the dynamical characteristics of spin current-driven devices via their interaction with external signals; 3) The role of quantum magnetization fluctuations in the interaction between the magnetization and the spin-polarized current.

An emerging promising type of spintronic devices for microwave applications is the Spin Hall nanooscillator (SHNO). In SHNO, microwave-frequency magnetization dynamics is excited in an "active" nanomagnet by pure spin current generated by the spin Hall effect. In this work, it is shown that spectral, thermal and electrical properties of SHNO can be enhanced by optimizing the geometry of the nanodevice. In particular, increased current concentration in a small region, achieved by nanopatterning the spin-Hall material (the source of spin current), reduces the current required for the device operation. Moreover, the reduced area of interface between the spin Hall material and the active nanomagnet improves the spectral properties of the device. In addition to modifying geometry of spin Hall layer to modify properties of spin Hall nanooscillator. In addition, a new type of SHNO is experimentally demonstrated in this work. It is based on a bilayer of spin Hall material and active layer nanopatterned into a bow-tie nanoconstriction. Theoretical analysis and micromagnetic simulations performed in this work demonstrate the importance of nonlinear dynamical mechanisms, dipolar magnetic fields, and the Oersted field of the current for the spatial and spectral characteristics of the studied structures.

The presented work also addresses the dynamical stability and coherence of SHNO, by studying their interaction with external microwave signals. It is shown that strong dynamical nonlinearity of SHNO is responsible both for their limited coherence and their ability to efficiently synchronize with

external microwave signals. The synchronization is shown to dramatically improve the spectral characteristics of SHNO, and is possible in a wide range of temperature and frequencies. The demonstrated synchronization of SHNO opens a way for the development of arrays of mutually synchronized oscillators with improved microwave generation characteristics.

The last part of this work addresses the fundamental mechanisms of interaction between the magnetization and the spin polarized currents. The present understanding of the underlying mechanism, called the spin transfer effect, is based on the classical approximation for the magnetization. In this work, the theory of spin transfer is extended to include the quantum-mechanical description of magnetization. The central result of the presented work is the prediction of spin transfer due to quantum magnetization fluctuation, and its experimental demonstration in a nanomagnetic system. Both the analysis and the presented measurements demonstrate that quantum fluctuations provide the dominant contribution to spin transfer at cryogenic temperatures, and their role remains significant even at room temperatures. Multiple consequences for the magnetoelectronic phenomena in ferromagnetic and antiferromagnetic systems are predicted based on these results.

Effect of spin current on magnetization dynamics

by

Andrei Zholud

M.S., National Academy of Sciences of Belarus, 2010

B.S., Belarusian State University, 2009

Advisor: Sergei Urazhdin, Ph.D.

A dissertation submitted to the Faculty of the
James T. Laney School of Graduate Studies of Emory University
in partial fulfillment of the requirements for the degree of
Doctor of Philosophy
in Physics
2017

Acknowledgments

First of all, I would like to thank my advisor Dr. Sergei Urazhdin for great mentoring and support during my graduate study. He helped me to develop scientific and research skills, which will be very valuable in my future career. Also I would like to thank all my committee members Dr. Phillip First, Dr. Justin Burton, Dr. Khalid Salaita, Dr. Stefan Boettcher, Dr. Hayk Harutyunyan for their valuable advices during time of PhD research.

I had wonderful time doing research at Urazhdin's lab, I would like to thank all lab members for a great time and help. In particular I thank postdocs Dr. Weng Lee Lim, Dr. Rongxing Cao, Dr. Ronghua Liu and graduate student Ryan Freeman, Dr. Phillip Tabor and Guanxiong Chen. I thank to electronic coordinators Lowell Ramsey and Dr. Josh Savory for their help in design and troubleshoot electronic circuits. I thank machine shop staff Cody Anderson and Horace Dale for making complex parts for my experiments. I thank Dr. Ajit Srivastava and Dr. Connie Roth for using their lab equipment.

Also I would like to thank all Emory physics graduate student and Young Emory Physicist, especially Dr. Skanda Vivek, John Kirkham, Roman Bagley, Dr. Laura Gray, Dr. Justin Pye, Dr. Trent Burson, Benjamen Nforneh, Dr. George Leung, Ryan Freeman, Xinru Huang, Baohua Zhou, Robert Lemasters, Emrah Simsek, Tyler Smith, Michael Thees, Dr. Vijay Singh, Guga Gogia, Catalina Rivera, Joseph Natale, Yan Yan, Dr. Xiang Cheng for their help and having fun together. I thank Calvin Jackson, Barbara Conner, Susan Cook, Sharon Jordan, Jason Boss and Ark Kleyman. I am grateful to the Emory University for this great opportunity to do research one of the best research facility in the world and be a part on wonderful Emory community.

Financial support for this research was provided by the National Science Foundation Grants ECCS- 1509794, ECCS-1305586, DMR-1218414 and DMR-1504449.

Contents

---

[1] Published article: V.E. Demidov, H. Ulrichs, S.V. Gurevich, S.O. Demokritov, V.S. Tiberkevich, A.N. Slavin, A. Zholud S. Urazhdin, "Synchronization of spin Hall nano-oscillators to external microwave signals". Nat. Comm. 5, 3179 (2014).

List of Figures

Citations to Previously Published Work

Chapter 2 contains research from two publications:

1. A. Zholud, S. Urazhdin, "Microwave generation by spin Hall nanooscillators with nanopatterned spin injector" *Appl. Phys. Lett.* **105**, 112404 (2014)

2. V. E. Demidov, S. Urazhdin, A. Zholud, A. V. Sadovnikov, S. O. Demokritov, "Nanoconstriction-based spin Hall nanooscillator", *Appl. Phys. Lett.* **105**, 172410 (2014)

Chapter 3 contains research from one publication:

3. V. E. Demidov, H. Ulrichs, S. O. Demokritov, S. V. Gurevich, V. Tiberkevich, A. Slavin, A. Zholud, S. Urazhdin, "Synchronization of spin Hall nano-oscillators to external microwave signals", *Nature Comm.* **5**, 3179 (2014)

Chapters 4 and 5 are based on one manuscript:

4. A. Zholud, R. Freeman, R. Cao, A. Srivastava, S. Urazhdin, "Spin transfer due to quantum fluctuations of magnetization", Submited to *Phys. Rev. Lett.*, (2017)

Published work not included in this dissertation:

5. V. E. Demidov, S. Urazhdin, A. Zholud, A. V. Sadovnikov, A. N. Slavin, S. O. Demokritov, "Spin-current nano-oscillator based on nonlocal spin injection", *Sci. Rep.* **5**, 8578, (2015)

6. V. E. Demidov, S. Urazhdin, A. Zholud, A. V. Sadovnikov, and S. O. Demokritov, "Dipolar field-induced spin-wave waveguides for advanced magnonics" *Appl. Phys. Lett.* **106**, 022403 (2015)

Chapter 1

Introduction

1.0.1 Motivation

The rapid growth of information technologies increases demand on information storage and processing, setting challenging goals for science and technology. Modern silicon-based electronics is reaching its fundamental limits dictated by the laws of thermodynamics, statistical, and quantum mechanics [10, 11], which become important when electronic components contain only a few hundred atoms and cannot be treated as classical continuous media. Moreover, the complexity of the manufacturing process and its cost are increasing with the decreasing size of electronics components. To overcome these issues faced by modern electronics, research and development of new approaches, systems, and materials are required. For instance, plasmonics, one of several rapidly growing fields aimed at addressing these issues, allows one to optically encode and transmit information by coupling light with charge dynamics [12, 13]. Another example is spin-based electronics — spintronics [14, 15], which is the subject of this work. It is well known that electron besides charge has additional degree of freedom - the spin. By utilizing electron spin, it may be possible to develop new logic devices with low power consumption and short response time, as well as a new types of nonvolatile memory [16–20]. Operation of many types of spintronic devices relies on electrical current flowing through magnetic materials, which in this context can be thought of as ordered electron spin systems. The interplay between individual electron spins and the collective spin-dynamical states in magnetic systems, called the spin waves, can provide a useful approach for the control of spin degree of freedom. The spin wave quantum, the magnon, has been proposed as a carrier of information for the novel type of devices, called the magnonic devices [21, 22]. The potential applications of spintronics motivate a significant interest in the scientific and engineering communities. However, not all the fundamental or practical aspects of spin physics in materials are well understood.

In this work, I address the fundamental aspects of interaction between spin current and magnetic materials, and develop approaches for enhancing the efficiency of spin current-driven spintronic devices. In the introductory Chapter 1 I briefly explain the basic concepts of electron spin and spin current, magnetic ordering, and magnetization dynamics. I also describe measurement techniques used in my experimental research. This introduction should enable the reader to follow the results presented in the subsequent Chapters. In Chapter 2, I present the research into ways to improve the characteristics of spin Hall nano-oscillators (SHNO) - magnetic nanodevices in which coherent magnetization oscillation is excited by pure spin current generated by the spin Hall effect. I show that spectral, thermal and electrical properties of SHNO can be enhanced by optimizing the geometry of the nanodevices. Chapter 3 is focused on the interaction of SHNO with external signals. In particular, I show that the coherence of oscillation of SHNO can be enhanced by synchronizing them to external microwave signals. The synchronization of SHNO opens a way for the development of arrays of mutually synchronized spintronics devices for improved generation of coherent microwave radiation.

Further improvement of spintronic devices requires a better fundamental understanding of interaction between spin currents and magnetic systems. The present understanding of spin transfer is based on the classical approximation for the magnetization, even though the spin-polarized electrons mediating spin transfer are treated quantum-mechanically. In Chapter 4, I develop a quantum-mechanical extension of spin transfer theory, by analyzing the interaction between the magnetization and the electron spin, both of which are treated quantum-mechanically. Chapter 5 describes experimental confirmation of the quantum theory of spin transfer described in Chapter 4. These measurements showed that quantum magnetization fluctuations provide the dominant contribution to spin transfer at cryogenic temperatures, and their role remains significant even at room temperature. Multiple consequences for the magnetoelectronic phenomena in ferromagnetic and antiferromagnetic systems are predicted based on these results.

1.1 Magnetization dynamics and spin waves

1.2 Electron spin and spin current

In addition to charge, the electron has another fundamental property – the spin, or equivalently the intrinsic angular momentum, and the associated magnetic moment. The electron's spin $s = 1/2$ can have two possible values of projection on a given axis, $s_z = \pm\frac{1}{2}$. The corresponding projections of angular momentum are $\hbar/2$ or $-\hbar/2$. The intrinsic magnetic moment of electron, associated with its spin, is illustrated as a classical vector in Fig. 1.1. The magnetic moment of electron $m = \mu_B$ – the Bohr magnetron – is proportional to the spin, $m = \gamma S$, where γ for electron is the gyromagnetic ratio. The gyromagnetic ratio defines the ratio between the magnetic and the angular momentum of electron $\gamma = g\frac{q}{2m}$, where $g \approx 2$ dimensionless g-factor, q is the charge and m is the mass. The spin of electron was experimentally observed in 1922 by Stern and Gerlach in their experiment with silver atoms traveling through a strongly inhomogeneous magnetic field.

Electrical current is defined as the rate of flow of charge. Similarly to the electrical current spin current can be defined as the flow rate of spin. The main difference between the electrical and the spin current is that charge is a scalar quantity, and that it is conserved. On the other hand spin is a vector quantity, and in general it is not conserved. For example, spin-orbit interaction results in the conversion between spin and orbital angular momentum. Electrical current in which the numbers of spin-up and spin-down electrons are not equal, is called spin-polarized current. It carries an associated spin current. However, it is possible to produce a spin current without an associated electrical current. In this case, it is called a pure spin current. Imagine that spin-up

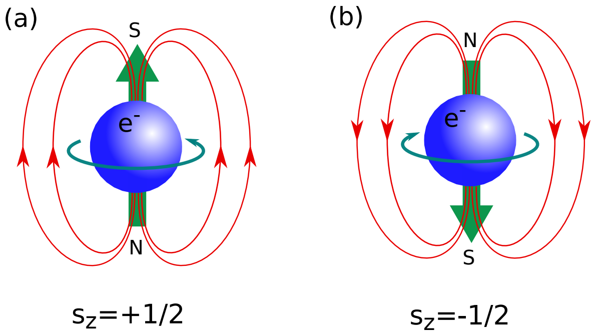

Figure 1.1: Illustration of electron spin as a classical magnet with north pole pointing down (a) for $s_z = +1/2$ or up (b) for $s_z = -1/2$.

electrons move in one direction, while spin-down electron move in the opposite direction, as shown is Fig. 1.2. The numbers of electrons with spin-up and spin-down are equal, so the total electrical current is zero, but the spin current is not.

Since the spin is not conserved, there is no corresponding spin continuity equation, so the definitions of spin current vary [19, 23–25]. For example, Zhou *et al.* [26], starting with continuity equation $\frac{\delta\rho}{\delta t} + \nabla j = 0$ and multiplying it by the spin $\mathbf{s}(\frac{\delta\rho}{\delta t} + \nabla j) = 0$, defines the spin current density as: $J_s := \mathbf{js}$, which "is a measurable 2-rank real pseudotensor". Shi *et al.* [23] derive the continuity equation in systems with spin-orbit coupling: $J_S = \sigma E - D_S \nabla S$, where σ is the spin Hall conductivity.

1.2.1 Magnetic order and magnetization dynamics

Types of magnetic materials

All materials can be separated into two classes according their magnetic properties: i) materials without permanent microscopic magnetic moments (called diamagnetics or paramagnetics), and ii) materials with permanent magnetic moment. The second class of materials can be separated into several sub-classes according to their magnetic ordering. The most common types or magnetic ordering are ferromagnetic, ferrimagnetic and antiferromagnetic. The ordering appears below a certain critical temperature, due to exchange interaction between neighboring spins. On the other

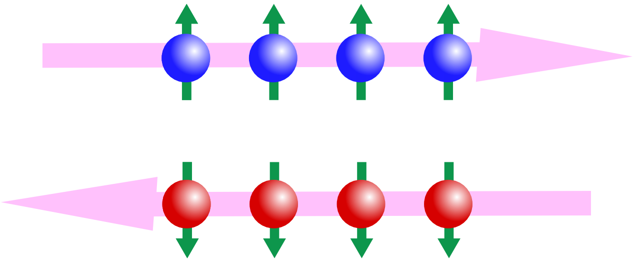

Figure 1.2: Electron with opposite spins moving in opposite direction, creating zero net charge transfer.

hand, in paramagnets, non-zero magnetization can be induced by external magnetic field [Fig. 1.3].

Below I will focus on ferromagnetic materials, and for simplicity will call them just magnetic materials. One of the characteristic of magnetic material is magnetization. Magnetization $\vec{M}$ is a vector, which describes the density of magnetic moments in the material: $\vec{M} = \frac{\sum \vec{m_i}}{V}$, where $\vec{m_i}$ is an elementary magnetic moment and V is volume. As the magnetization is not always uniform across the body and can vary among different regions, it is useful to express it as a ratio of the elementary magnetic moment dm over the elementary physical volume dV: $\vec{M} = \frac{d\vec{m}}{dV}$.

1.2.2 Magnetization dynamics

Magnetic material can be considered as a collection of microscopic magnetic moments (or spins). To understand the dynamics of magnetization, I start by analyzing the dynamics of a single magnetic moment (spin) in external magnetic field, and then extend the analysis to the ordered spin systems.

Larmor precession

As it was discussed above electron posses magnetic dipole moment $m = \mu_B$ due to its intrinsic angular momentum s or spin. When magnetic dipole is placed into external magnetic $\vec{B}$ which is not collinear with the direction of magnetic dipole moment, magnetic field attempts align magnetic

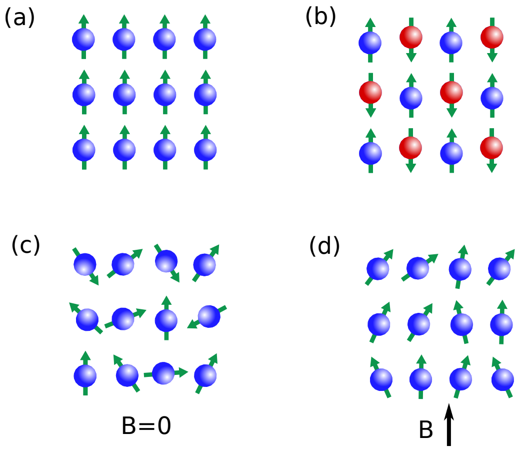

Figure 1.3: Different types of magnetic ordering: ferromagnetic (a), antiferromagnetic (b), paramagnetic in the absence (c) and in the presence (d) of magnetic field.

dipole along its direction exerting torque $\tau = -\mu_B \times \vec{B} = -\gamma \vec{S} \times \vec{B}$ [Fig. 1.4]. Exerted torque changes angular momentum causing precession of magnetic moment around direction of external magnetic field. This precession is called Larmor precession. The frequency of Larmor precession is proportional to external magnetic field $\omega_{LP} = -\gamma \vec{B}$.

Because spin of electron is a quantum characteristic it is required quantum description. Dynamics of electron spin is described by spinor χ, which is a solution of Schroedinger equation with Hamiltonian $H = -\gamma \mathbf{S} \cdot \mathbf{B}$:

$$ih\frac{\delta\chi}{\delta t} = \mathbf{H}\chi \tag{1.2.1}$$

The general solution for time independent Hamiltonian can be expressed in terms of stationary states [27]:

$$\chi(t) = \cos(\Theta/2)\chi_+ e^{\frac{-iE_+ t}{\hbar}} + \sin(\Theta/2)\chi_- e^{\frac{-iE_- t}{\hbar}} = \begin{pmatrix} \cos(\Theta/2)e^{\frac{-iE_+ t}{\hbar}} \\ \sin(\Theta/2)e^{\frac{-iE_- t}{\hbar}} \end{pmatrix} \tag{1.2.2}$$

where Θ angle of precession (tilt angle between direction of field and spin).

To describe spin dynamics it is necessary to calculate the expectation values of three components

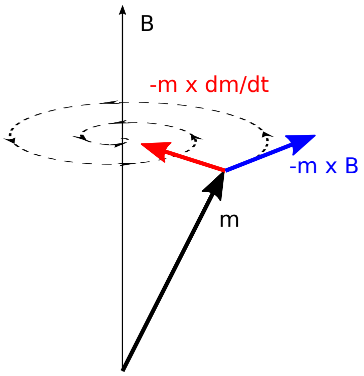

Figure 1.4: Precession of magnetic moment around magnetic field.

of spin **B**:

$$\langle S_x \rangle = \langle \chi | \mathbf{S_x} | \chi \rangle = \frac{\hbar}{2} \sin\Theta \cos(\gamma B t) \tag{1.2.3}$$

$$\langle S_y \rangle = \langle \chi | \mathbf{S_y} | \chi \rangle = -\frac{\hbar}{2} \sin\Theta \sin(\gamma B t) \tag{1.2.4}$$

$$\langle S_z \rangle = \langle \chi | \mathbf{S_z} | \chi \rangle = \frac{\hbar}{2} \cos\Theta \tag{1.2.5}$$

The physical meaning of these expectation values is that spin precesses around z axis with angular speed $\omega = \gamma B$.

Ferromagnetic resonance

Torque exerted by external magnetic field on magnetic moment is equal to change of angular momentum $\mathbf{L}$ of magnetic dipole with time: $\tau = \frac{d\mathbf{L}}{dt}$. As it was mentioned above gyromagnetic ratio γ defines direct proportionality between magnetic moment to angular momentum, and torque is given by cross product of magnetic field and magnetic moment:

$$\frac{d\mathbf{m}}{dt} = \gamma \mathbf{m} \times \mathbf{H} \tag{1.2.6}$$

This equation describes precession of magnetization around external magnetic field in stationary state without losses. In real systems magnetic moment usually interacts with other parts of a system such as spins, electrons and lattice. These interactions cause energy loss and magnetic moment relaxes to the direction of external magnetic field. The relaxation of magnetization is described by damping term, which should be added to Eq. (1.2.6) [Fig. 1.4]. Landau and Lifshitz introduced dissipative term as additional effective torque, which tries to align magnetic moment with external field: $-\frac{\lambda}{M_S}\mathbf{m} \times (\mathbf{m} \times \mathbf{H})$, where λ is phenomenological constant characteristic of a material and M_S is magnetization saturation. On the other hand Gilbert [28] proposed to treat dissipation as a "viscous force", which is proportional to time derivative of magnetization similar as viscous force proportional to velocity: $\frac{\alpha}{M_S}\mathbf{m} \times \frac{\partial \mathbf{m}}{\partial t}$, where $\alpha > 0$ is Gilbert damping constant [29], which depends on material properties. Therefore, the precessional equation, which describes magnetization dynamics with dissipation, is called Landau-Lifshitz-Gilbert (LLG) equation:

$$\frac{d\mathbf{m}}{dt} = -\gamma \mathbf{m} \times \mathbf{H} + \frac{\alpha}{M_S}\mathbf{m} \times \frac{\partial \mathbf{m}}{\partial t} \tag{1.2.7}$$

Magnetization of material can be considered as collection of interacting magnetic moments. The lowest frequency mode, when all magnetic moments precess in phase, is called ferromagnetic resonance (FMR) mode or uniform mode. The frequency of FMR mode for film magnetized in-plane can be calculated by Kittel [30] formula:

$$f = \frac{\gamma}{2\pi}\sqrt{B(B + \mu_0 M)} \tag{1.2.8}$$

Beside uniform precession of magnetization nonuniform modes are possible too. These nonuniform modes are called spin waves, and their equivalent quasi-particles are magnons. There are two main interaction mechanics between spins: long range dipole-dipole interaction and short range exchange interaction. The exchange interaction has purely quantum nature and arises from Pauli's exclusion

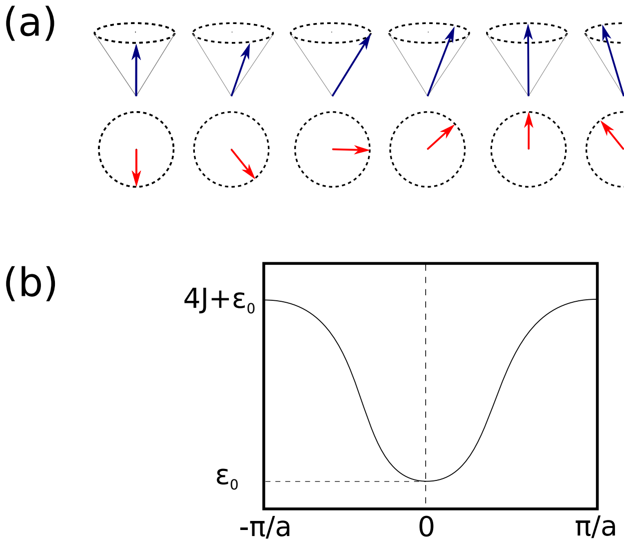

Figure 1.5: (a) Spin wave in one dimensional spin chain. (b) Spin wave dispersion for one dimensional chain.

principle. According Pauli's exclusion principle no two fermions can occupy same quantum state simultaneously.

To illustrate dynamics of spin wave it is necessary consider one-dimensional ferromagnetic chain, which is shown in Fig. 1.5(a). The exchange interaction between neighboring spins $\mathbf{S_1}$ and $\mathbf{S_2}$ is described by Heisenberg Hamiltonian: $H = -2\frac{J_{ex}}{\hbar^2}\mathbf{S_1} \cdot \mathbf{S_2}$, where J_{ex} is an exchange constant. For the chain of N spins with nearest neighbors interaction Hamiltonian is: $H = -2\frac{J_{ex}}{\hbar^2}\sum \mathbf{S_n} \cdot \mathbf{S_{n+1}}$.

The solution of Schroedinger equation with Hamiltonian for a spin chain provides the following expression for the expected energy is $\epsilon = 2J_{ex}(1 - \cos ka) + \epsilon_0$, where a in distance between spins and k is a wave vector. The dispersion relation for spin waves for one dimensional chain is shown in Fig. 1.5(b). Spin wave can be interpreted as excitation, when precession phase of each spin varies linearly along the chain [Fig. 1.5(a)].

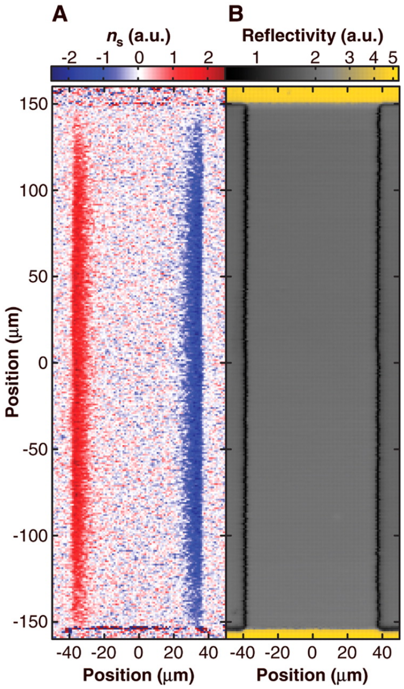

Figure 1.6: Experimental observation of spin density distribution in GaAs due to SHE. Reproduced for Ref. [1].

1.2.3 Spin Hall effect

One of the source of pure spin current is spin Hall effect (SHE). SHE was theoretically predicted by Dyakonov and Perel [31,32] and experimentally observed in GaAs by Kato *et al.* [1]. This effect consists of appearance of spin current transverse to electron flow and accumulation of opposite spin on opposite boundaries [Fig. 1.6]. In contrast to ordinary Hall effect, SHE does not require external magnetic field. The origin of SHE is spin-orbit (SO) interaction — coupling of electron spin with its orbital motion.

SHE is observed in materials with strong SO scattering of conduction electrons and does not require magnetic fields. Instead, the role of the effective magnetic field is played by the SO interaction, resulting in an effective spin-dependent Lorentz force. Since the direction of this force is opposite for electrons with opposite spins, the net electric current is parallel to the electric field,

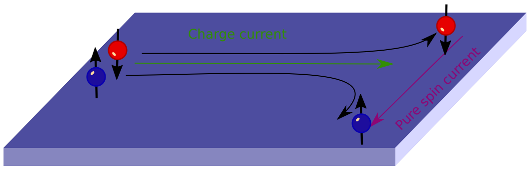

Figure 1.7: Schematic of spin Hall effect.

but there is a net spin current flowing perpendicular to it [Fig. 1.7]. Spin current sufficient for the operation of spintronic devices can be generated at moderate charge currents in efficient SHE materials such as platinum or tantalum [33–35].

1.3 Spin transfer torque

Electron moving through magnetic material can exchange its spin with magnetization in such way that total angular momentum is conserved. Slonszewski [36] had demonstrated that electrons can transfer its angular momentum to magnetization. This effect is called spin transfer torque (STT). STT can excite magnetization dynamics or even reverse magnetization. Slonczewski considered the scattering of spin-polarized electrons at the interface between ferromagnet (FM) and a non-magnetic material. In idealized case when FM is a perfect spin polarizer, it transmits only the majority electrons whose magnetic moment is parallel to the magnetization $\vec{M}$ of FM. The minority electrons whose magnetic moment is anti parallel to the magnetization $\vec{M}$ are reflected by FM. However, when the spin-polarization of the incident electron is non-collinear with $\vec{M}$, the component of the electron spin normal to $\vec{M}$ becomes transferred to it upon scattering, because both the transmitted and the reflected components of the electron's wavefunction are polarized collinear to $\vec{M}$. The absorbed angular momentum associated with transverse polarization results in a torque exerted on $\vec{M}$.

The spin transfer (ST) can be separated into two terms: field-like torque and damping-like torque. The field-like torque is $\tau_F = \hbar \mathbf{J_S} \mathbf{m} \times \mathbf{s}$, where $\mathbf{J_S}$ is the dimensionless spin current flowing across the magnetic interface, $\mathbf{s}$ is a unit vector along its polarization, and $\mathbf{m}$ is a unit vector in the direction of magnetization. This torque typically results in a minor correction to the frequency of magnetization dynamics, and will be ignored here. The damping-like torque is $\tau_D = -\hbar \mathbf{J_S} \mathbf{m} \times [\mathbf{m} \times \mathbf{s}]$, which has the same form as the Landau damping torque $\tau_{GL} = -\alpha_{GL} \mu \mathbf{m} \times [\mathbf{m} \times \mathbf{H}]$. Here, α_{GL} is the Gilbert damping constant. For magnetic field H parallel to spin current polarization s, damping-like torque opposes Landau damping, resulting in reduction of the effective damping. At a critical value $\mathbf{J_S}_C = \frac{1}{\hbar} \alpha_{GL} \mu \mathbf{H}$, damping becomes compensated by ST, which can produce self-sustained magnetic dynamics or magnetization reversal [37–39].

1.4 Anisotropic magnetoresistance

Magnetoresistance is a property of materials to change its electrical resistance in external magnetic field. Anisotropic magnetoresistance (AMR) is a dependence electrical resistance on angle between the direction of electrical current and the direction of material magnetization. This effect arises from SO interaction and magnetization. For 3d ferromagnets like permalloy (Py) AMR is maximal when magnetization is parallel to electrical current, and minimal when it is perpendicular. In many material AMR depends only on angle between current and magnetization and follows the equation:

$$\rho(\alpha) = \rho_\perp + \Delta\rho \cos^2 \alpha \tag{1.4.1}$$

where $\Delta\rho$ is the difference between maximal and minimal values of AMR. Figure 1.8 shows typical dependence of resistance on angle between current and magnetization of Py.

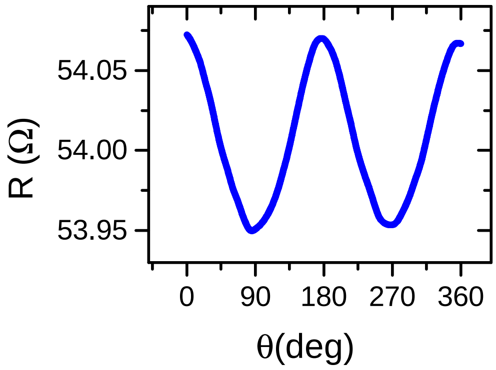

Figure 1.8: Dependence of resistance on angle between current and magnetic field in Py.

1.5 Giant magnetoresistance

The other type of magnetoresistance is a giant magnetoresistance (GMR). GMR effect is observed in multilayer structures, where two FM layers are separated by thin nonmagnetic material. GMR effect first was discovered in Fe/Cr/Fe structure with antiferrromagnetic coupling between two FM layer by Grunberg and Fert independently [40, 41]. Electrical resistance of GMR structure depends of relative orientation of magnetization of FM layers [42]. For example, when two layer are antiferromagnetically coupled and oriented anti parallel, the GMR structure has high resistance. If external field strong enough to align magnetization of both layer in parallel configuration is applied, GMR structure has low resistance [Fig. 1.9].

The difference of resistance between parallel and anti parallel configuration can be 10's % of the total resistance of structure. This change of resistance is "giant" compared to AMR, where change of resistance is only around 1% [43]. The first experiment of GMR measurement was performed in a current in plane (CIP) structure. However, structures with current perpendicular to plane (CPP) geometry have larger GMR compared to CIP [44]. The geometry of CPP and larger GMR make CPP GMR structures more attractive for technological and research application. The total resistance of GMR structure is:

$$R(\Theta) = R_0 + \Delta R \sin^2 \frac{\Theta}{2}, \tag{1.5.1}$$

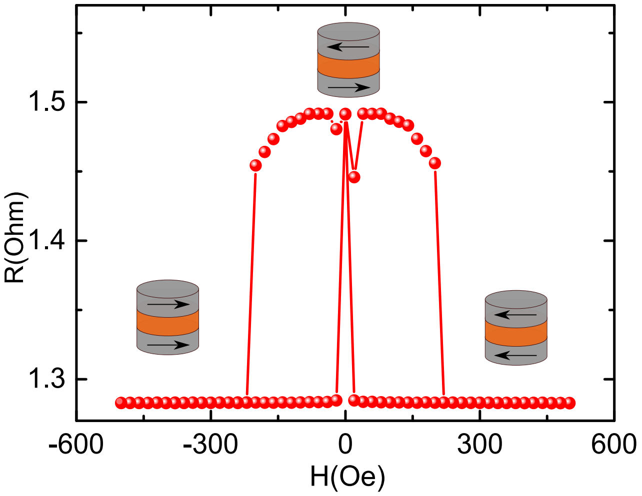

Figure 1.9: Dependence of resistance on magnetic field for Py/Cu/Py spin valve.

where R_0 is the resistance of GMR structure in parallel configuration, ΔR is the difference between maximal and minimal resistance, and Θ is the angle between magnetization direction of two magnetic layers.

The effect of GMR arises from spin dependent scattering in ferromagnetic materials. In parallel configuration of both magnetic layers [Fig. 1.10(a)] electron with spin antiparallel to magnetization has higher probability of scattering in both magnetic layers. In contrast, electron with spin parallel to magnetization experiences less scattering in both layers. When magnetization of both layers is antiparallel to each other [Fig. 1.10(b)] electrons with both spin orientations experience equal amount of scattering.

To explain resistance dependence on magnetization orientation the resistor model of GMR spin valve is usually used [Fig. 1.11]. The resistivity of GMR structures is described by using two conductivity channels: i) when spin magnetic moment is parallel to magnetization, channel has low resistance $R_{\uparrow\uparrow}$, ii) when spin magnetic moment is antiparallel to magnetization, channel has high resistance $R_{\downarrow\uparrow}$. In CPP GMR geometry [Fig. 1.11(a)] channel for electrons with particular orientation is represented as two resistors in series, and two channels for electrons with spins up and

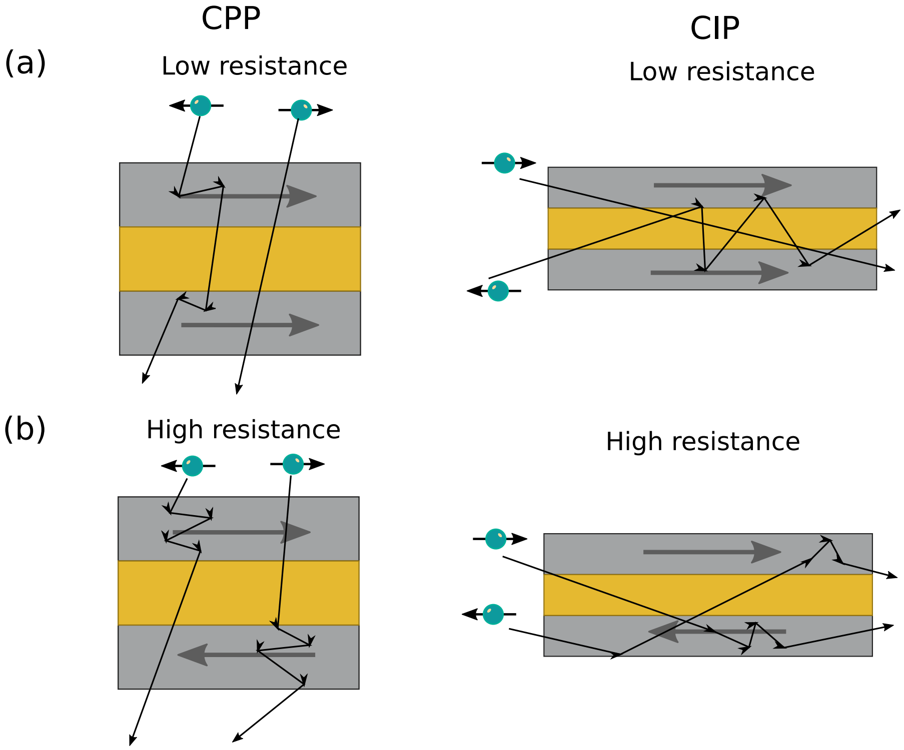

Figure 1.10: Schematic of spin-dependent scattering in CPP and CIP geometries when (a) magnetization of both layers parallel and (b) anti parallel.

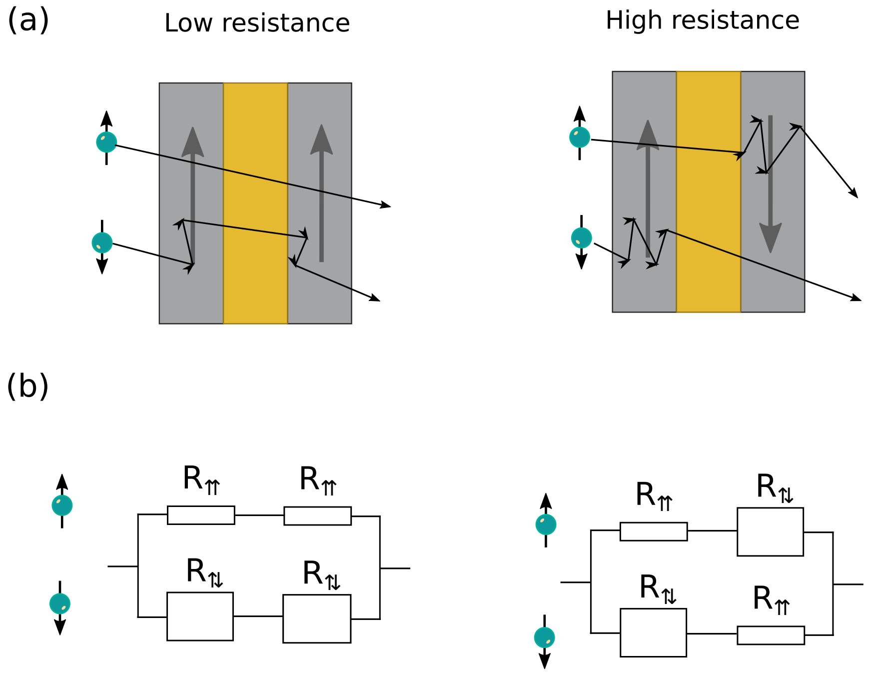

Figure 1.11: (a) Schematic of electron scattering and (b) equivalent resistor circuit of GMR spin valve for hight and low resistive states.

down are presented as resistors in parallel [Fig. 1.11(b)]. The total resistance of GMR structure for parallel configuration is $R_P = \frac{2R_{\uparrow\uparrow}R_{\downarrow\uparrow}}{R_{\uparrow\uparrow}+R_{\downarrow\uparrow}}$ and for antiparallel configuration is $R_{AP} = \frac{R_{\uparrow\uparrow}+R_{\downarrow\uparrow}}{2}$.

1.6 Experimental techniques

1.6.1 Measurements

Lock-in measurements

Lock-in is phase-sensitive low-noise measurement of AC signals, which allows to measure both amplitude and phase of a signal. An external reference signal with frequency ω_{ref} excites a voltage response in the sample. Lock-in detects the response signal of the system to the reference signal, which has a phase-shift Θ_{sig} relative to the reference signal [Fig. 1.12]. Lock-in also generates an internal signal with frequency ω_L and phase Θ_{ref}. It multiplies input signal from the sample and the internal signal by multiplier. The product of two signals is just product of two sinusoids:

$$\begin{aligned} V = V_{sig}V_L = (V_{sig_0})\sin(\omega_r t + \Theta_{sig})(V_{L_0})\sin(\omega_L t + \Theta_{ref}) = \\ = \frac{1}{2}V_{sig_0}V_{L_0}(\cos((\omega_r - \omega_L)t - (\Theta_{sig} - \Theta_{ref})) \\ - \cos((\omega_r + \omega_L)t + (\Theta_{sig} + \Theta_{ref}))) \end{aligned} \tag{1.6.1}$$

The resultant AC signal is converted to a DC signal by time-averaging of the lock-in. After time-averaging, the final signal is not zero only if $\omega_r = \omega_L$ and its amplitude is given by:

$$V_{dc} = \frac{1}{2}V_{sig_0}V_{L_0}\cos(\Theta_{sig} - \Theta_{ref}) \tag{1.6.2}$$

The reference phase Θ_{ref} of lock-in is tunable, and it is convenient to make it zero. In this case, the final signal is a product of the detected and lock-in signals amplitudes multiplied by cosine of the signal phase.

Most of the modern lock-in amplifiers can measure not only amplitude of the detected signal but also phase of the signal Θ_{sig}. For this purpose lock-in has a second multiplier. It multiplies the detected signal by shifted by $\pi/2$ lock-in signal. After averaging:

$$V_{dc} = \frac{1}{2}V_{sig_0}V_{L_0}\sin(\Theta_{sig}) \tag{1.6.3}$$

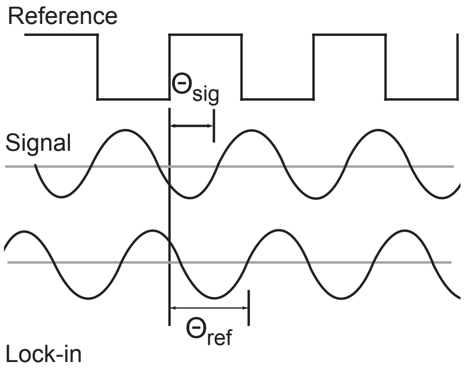

Figure 1.12: Schematic representation of the signal phase [2]

Lock-in amplifier has two output signals, one of them is proportional to $\cos(\Theta_{sig})$ ('in-phase' component or just X), and the second is proportional $\sin(\Theta_{sig})$ ('quadrature' component or just Y) [2]. If the two components of the signal are known, it is easy to find the phase of detected signal:

$$\Theta_{sig} = \arctan \frac{Y}{X} \tag{1.6.4}$$

Micro focused Brillouin light spectroscopy

Brillouin light spectroscopy (BLS) is a powerful technique for probing low energy vibrational and magnetic excitations. Brillouin Light Scattering is an inelastic scattering of light on acoustic phonons, which was predicted by Brillouin in 1922 [45] and named in his honor. BLS is usually used to study phonons [46, 47], magnons [48, 49] and other low energy (frequency) propagating excitations. In condensed matter physic the excitations of the media can be associated with order parameters such as density (for phonons) or magnetization (for magnons) fluctuations, which can scatter incident light inelastically. As excitations propagate in the media, the frequency shift can be described as a Doppler shift of the frequency of incident light on running waves. However, in many cases, it is more convenient to use a quantum description to obtain the relation between frequencies of scattered light and frequencies of excitation. In quantum language particles of light, photons, interact with particles of the media, phonons or magnons. In the process of inelastic scattering an incident photon with frequency ω transfers part of its energy to the phonon/magnon. As a result the frequency of the scattered photon becomes smaller, with $\omega_S < \omega$, where ω_S is the Stokes component. In the case when the scattered photon gains energy from the phonon/magnon, the frequency of photon increases, $\omega_{AS} > \omega$, where ω_{AS} is the anti-Stokes component.

Collectively, the spectrum of scattered light also contains several new frequencies corresponding to the Stokes component ω_S and anti-Stokes component ω_{AS}, beside the incident photon frequency ω.

Knowing the frequencies of incident and scattered photons, the frequency of phonon/magnon $\Delta\omega_B$, called the Brillouin frequency, can be determined:

$$\Delta\omega_B = |\omega - \omega_{S,AS}|. \tag{1.6.5}$$

Figure 1.13 shows energy and momentum diagrams of the BLS process.

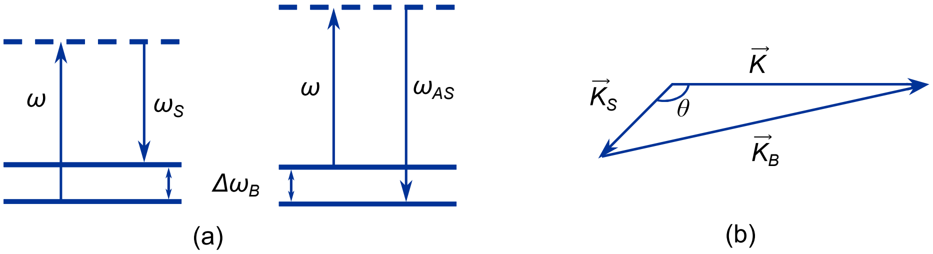

Figure 1.13: Energy (a) and momentum (b) diagrams in BLS process. ω, $\omega_{S,AS}$ and ω_B frequencies of incident, scattered photons and frequency of phonon/magnon. Θ — an angle between incident and scattered photons.

The regular frequency shift in BLS is in a range of $\sim$ 0.5-50 GHz [50]. Since the shift can be small, monochromatic incident beam with narrow spectral line and optics with high resolution are therefore required.

The angle between scattered and incident photons depends on the momentum of the phonon/magnon [Fig. 1.13 (b)]. Consequently, BLS also allows us to obtain the dispersion relation between the frequency of excitation and its wave vector $\vec{k}$ for phonons/magnons of different materials [51].

BLS is a powerful tool for probing the excitations such as phonons and magnons in materials and nanostructures. An example of the BLS spectrum of magnons in a thin film of cobalt is shown in Fig. 1.14. BLS allows to resolve different modes of magnons like surface magnons (DE peaks in Fig. 1.14) and surface standing magnons (peaks 1 and 2 in Fig. 1.14) The peaks with positive frequency shift correspond to transferring energy from excitation to light, while those with negative shifts corresponds to absorption of photon energy by excitations.

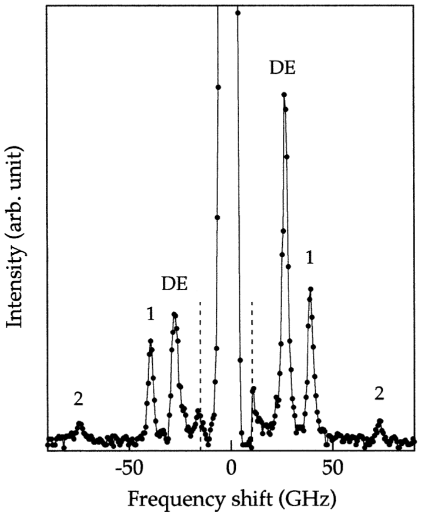

Figure 1.14: BLS example spectrum of magnons in cobalt film. Reproduced from Ref. [3].

The intensity of the peaks indicates scattering efficiency of excitations with particular frequency, where the scattering (peak) intensity is proportional to the density of excitation at that frequency.

The spatial resolution of BLS is on the order of tens of micrometers, which is defined by the diameter of the laser beam spot. Invention of BLS microscopy [52] with a laser beam focused to diffraction limit has increased resolution down to hundreds nanometers. In this method, a lens with high numerical aperture (NA) is used to focus laser beam on a sample [Fig. 1.15(a)]. Scattered light passes through the same lens. In this situation, the micro-BLS method automatically integrates over all wave vector up to some maximal value, which is defined by the numerical aperture of the lens. Due to integration over all wave vector micro-BLS loses its ability to resolve k-space.

The micro-BLS method is effectively used for mapping the surface magnon intensity distribution

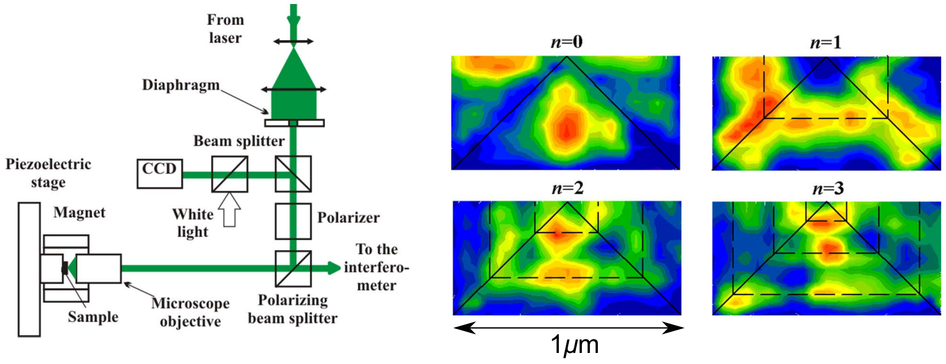

(a) (b)

Figure 1.15: (a) Schematic micro-BLS setup. (b) Distribution of magnons with different modes (n=0-3) in CoFe film, obtained with micro-BLS method. Figure reproduced from Ref. [4].

in microscale samples [Fig. 1.15 (b)].

Chapter 2

Electronic and spectral properties of SHNO

Spin Hall nano oscillators (SHNO) are a novel type of spintronic devices, where magnetization dynamics is excited by pure spin current from spin Hall effect. Demidov *et al.* [5] demonstrated that by increasing concentration of electrical current in a small region it is possible to achieve high spin current generation from spin Hall effect [Fig. 2.1(a)]. This pure spin current can be strong enough to excite coherent auto-oscillation of the magnetization of the magnetic layer [Fig. 2.1(b)].

These oscillations were detected by micro-BLS technique at room temperature. After that it was demonstrated that such devices can generate microwave signal at cryogenic temperatures [53]. The oscillation frequency is lower than FMR in Permalloy (Py), indicating that oscillation mode is a localized non-propagating soliton (bullet mode [54]). Also it was shown the line-width exponentially grows with increasing temperature. The power of microwave signal decreases as temperature increases as well, and become lower than thermal noise around $T = 240$ K.

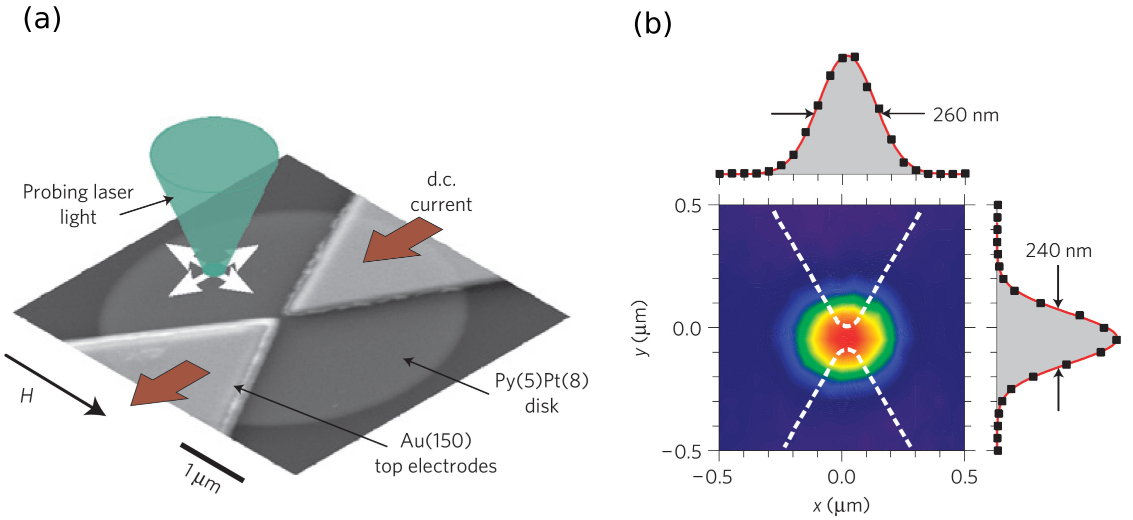

Figure 2.1: (a) Picture of SHNO device obtained with scanning electron microscopy. (b) Spacial map of oscillation distribution in active region of SHNO obtained with BLS technique. Figures reproduced from Ref. [5].

2.1 Geometry and operation of SHNO

Figure 2.1(a) shows SEM image of a typical SHNO device, based on planar point contact. The device is comprised of Py(5nm)/Pt(4nm) bilayer several micrometers in diameter. Two 100 nm thick top electrodes made from high conductive material (gold or copper) are placed on the top of bilayer disk. The small gap between sharp tips of the top electrodes is less then 100 nm. Such geometry of top electrodes allows to achieve high current density in the gap.

The general principle of operation of SHNO is shown in Fig. 2.2. The external magnetic field H set in-plane magnetization direction of Py layer. Electrical current flows predominantly through high conductivity top electrodes everywhere except small gap between them. In the gap current is injected into Py/Pt bilayer. Current flowing in plane in Pt layer produces transverse pure spin current, which is injected into Py layer. The pure spin current exerts torque on magnetization due to STT effect and magnetization starts precessing around external H field. Because of the high current density in the gap between two electrodes generated pure spin current is strong enough to

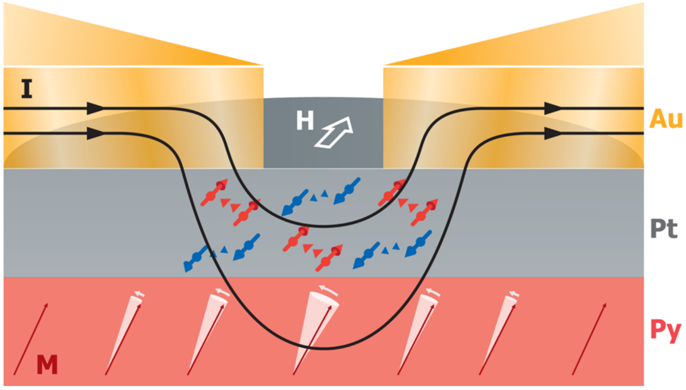

Figure 2.2: Schematic of current flow and spin current generation in SHNO. Figure reproduced from Ref. [6]

.

excite coherent oscillations of magnetization.

Those oscillations can be detected optically with micro-BLS or electronically. Electronic measurements rely on AMR in FM layer. Oscillating magnetization causes oscillation of the angle between magnetization and current. As the angle oscillates AMR signal also oscillates with the same frequency. Maximal amplitude of AMR oscillation is achieved when angle is 45°. On the other hand ST from SHE is the most significant when magnetization is orthogonal to the current. Therefore optimal angle for electronic measurements is 60°.

2.1.1 SHNO with patterned spin injector

Coherent magnetization oscillations excited by pure spin current in SHNO was observed at room temperature by BLS and at cryogenic temperatures by electronic microwave measurements. The intensity of microwave oscillations decreases with increasing temperature, and spectrum broadens quickly that microwave signal becomes completely suppressed above 240 K. Moreover, the electrical current required to excite oscillations is significantly larger than in traditional spin torque oscillators [55]. In this research I have demonstrated that issues mentioned above can be resolved by modifying geometry of spin injector of SHNO devices. The planar geometry of SHNO devices gives advantage of easy modification of the spin injector layer without alternating properties of the magnetic layer.

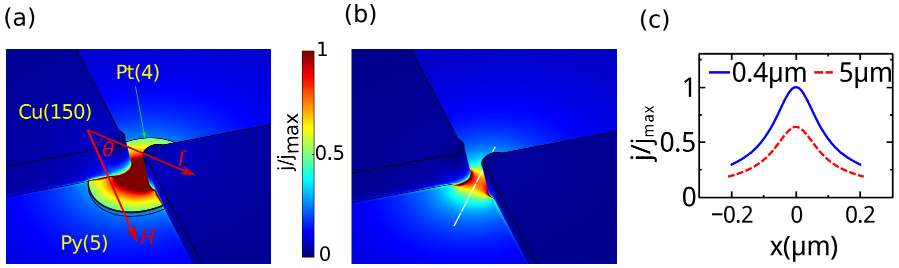

Figure 2.3: Current distribution in SHNO devices with different geometries calculated with COMSOL Multiphysics. (a) Current distribution in the device with patterned 400 nm in diameter Pt disk. (b) The same as in (a), but for extended 5 μm Pt layer. Both of calculated distribution normalized to the maximal current density j_{max} in the center of 400 nm Pt disk. (c) Calculated distribution through central cross section (dashed line in (b)) for the sample with extended Pt layer (dashed line) and patterned 400 nm Pt layer (solid line). Reproduced from [7], with the permission of AIP Publishing.

Device with patterned Pt spin injector layer has better spectral characteristics, including narrower line-width and higher amplitude of oscillations, and operated at lower current. Moreover, such device is able to generate microwave signal in a wide range ot temperatures from 6 K to room temperature.

The devices was fabricated on annealed sapphire substrate by combination of e-beam lithography, high vacuum magnetron sputtering and thermal evaporation techniques. Active magnetic layer was made from Py ($Ni_{80}Fe_{20}$) in a shape of disk with 5 nm thickness and 5 μm diameter. On top of magnetic layer concentric Pt disk of 4 nm thickness was deposited. Several devices with varying diameter of Pt from 300 nm to 5 μm were fabricated to investigate how size of spin injector affect properties of device. Top electrodes were made from 150 nm Cu thick, had triangular shape with vertices separated by 100 nm gap place in the center of Pt/Py disk [Fig. 2.3]. Additional sample with thin Pt space under electrodes was fabricated to demonstrate effect of Pt interface on magnetization dynamics. Figures 2.3(a) and 2.3(b) show current distribution in the gap between top electrodes for samples with expended 5 μm Pt layer and patter 400 nm Pt layer respectively. Current is predominantly concentrated in the gap between top electrodes, which produces strong pure spin current to excite coherent oscillations. Profiles of current distribution in both types of structures are identical [Fig. 2.3(c)], however in the sample with 400 nm Pt disk current is twice higher than in extended Pt layer. Moreover in device with the extended Pt layer spin current injected in wider area, but in device parented Pt layer spin injection is localized and constrained by size of 400 nm Pt disk. There higher concentration and localization of current in device with patterned Pt spin injector leads lower required current to excite magnetization oscillations. In addition this reduces size of the interface between Pt and Py. Previous study showed that interface of Pt with FM can increase damping and significantly affect properties of FM [56, 57].

Spectral properties of the devices were measured by electronic microwave spectroscopy which utilizes AMR to detect magnetization oscillations excited by current. External magnetic field $H = 500$ Oe was applied in plane of the device to control magnetization direction of active magnetic layer. The angle between magnetization and current was 60°, which allows to maximize effect of spin torque on magnetization and simultaneously microwave signals generation. To show effect of spin injector size on spectral characteristics measurements of devices with spin injectors from 300 nm to 5μm in diameter were performed. Figure 2.4 shows comparison of spectral and electrical characteristics of devices with two different sizes of Pt spin injector. For SHNO with the extended Pt layer $d = 5\mu$m oscillation peak appears around $I = 25$ mA [Fig. 2.4(a)]. The amplitude of the peak increases with increasing electrical current and reach its maximum value of 16 pW/MHz and minimal line width of 6.5 MHz at $I = 27.5$ mA. In contrast for SHNO with the extended $d = 5$ μm Pt disk, device with patterned $d = 400$ nm Pt disk has significantly larger oscillation amplitude of 56 pW/MHz, which is achieved at $I = 11.75$ mA almost twice lower for device with the extended Pt layer. The line-width of spectrum with maximal amplitude for SHNO with patterned Pt injector is 5.1 MHz [Fig 2.4(b)], which is not only 20% smaller compared to device with extended Pt layer. Figure 2.4(e) shows dependence of spectral properties (full width on half maximum (FWHM) and central frequency) for device with extended 5 μm Pt disk on current. Central peak frequency gradually red shifts with increasing current before the amplitude of oscillations achieves its maximal value at I_{max}. The shape of spectral line for current $I < I_{max}$ is described by Lorentzian shape, which corresponds to a thermally broaden single oscillation mode. After I_{max} frequency experience

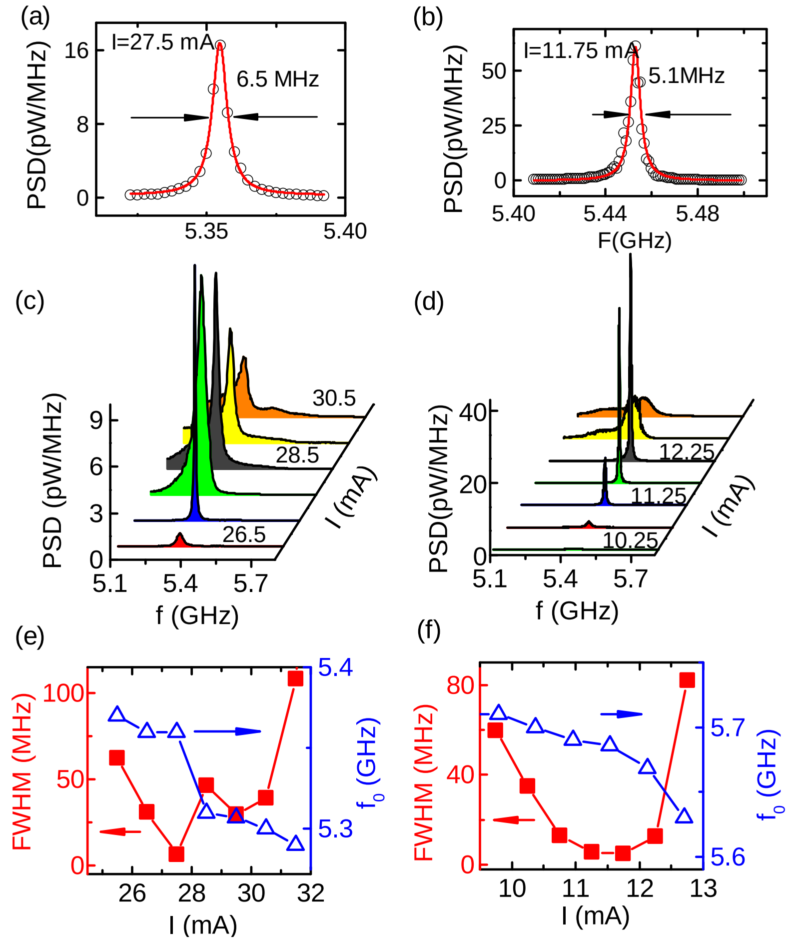

Figure 2.4: Comparison of spectral and electrical characteristics of SHNO with $d = 5\mu$m and $d = 400$ nm at $T = 6$ K. (a) Spectrum of SHNO with $d = 5\mu$m Pt disk acquired at $I = 27.5$ mA (symbols) and fitted with Lorentzian shape (solid line). (b) Spectrum of SHNO with $d = 400$ nm Pt disk acquired at $I = 11.75$ mA (symbols) and fitted with Lorentzian shape (solid line). (c) Dependence of spectrum on current for SHNO with $d = 5\mu$m Pt disk and (d) $d = 400$ nm Pt disk. (e) Dependence of full width in half maximum (solid symbols) and central frequency (open symbols) for SHNO with $d = 5\mu$ m Pt disk and (f) $d = 400$ nm Pt disk. Reproduced from [7], with the permission of AIP Publishing.

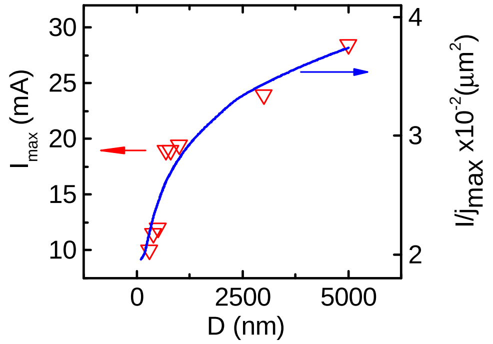

Figure 2.5: Dependence of current I_{max} corresponding to maximal amplitude of oscillations on diameter d of Pt disk. Symbols: Data obtained from experimental measurements. Solid line: Calculated current density in the center of Pt disk normalized to total current. Reproduced from [7], with the permission of AIP Publishing.

sudden larger red shift, line width broadens and amplitude decreases. At large currents shape of the spectral peak deviates from Lorentzian form, which is an evidence of excitation of multi-modal dynamics.

The main difference of the SHNO device with d = 400 nm Pt disk is significant decrease of oscillations currents [Fig. 2.4(d)], which is twice lower compared to the device with extended Pt layer. Figure 2.4(f) shows that frequency of oscillation peak gradually decreases in all range of current, which is an evidence that only single dynamical has largest contribution to oscillation and effect of other modes is reduces. The reasons for higher frequency modes have small effect on oscillations is that they are excited by higher current, have larger oscillation area. Localized spin current injection restricted by size of Pt disk reduces effect of extended propagating length which reduces coherency of oscillations [58].

Figure 2.5 illustrates how characteristic currents required to excite oscillation depend on size of Pt injector measured at $T = 6$ K. The current of maximal amplitude of oscillations I_{max} increase from 9.75 mA for 300 nm disk to 27.5 mA for 5 μm disk. These results are in good agreement with inverse of current density calculated with COMSOL in the center of Pt disk (solid line in Fig. 2.5).

As it was mentioned above amplitude of oscillations decreases and line width exponentially increases with increasing temperature for the device with extended 5 μm Pt layer and oscillations are completely suppressed for $T > 250$ K. This results are consistent with the results published before [53]. One of the main advantage of the SHNO device with reduced size of Pt spin injector is that line broadens not so fast with temperature and room temperature oscillations was observes in devices with $d < 800$ μm Pt spin injector. Figure 2.6(a) shows spectral properties for the device with $d = 400$ nm Pt spin injector at room temperature. Maximal amplitude of oscillations [Fig. 2.6(b)] is achieved at current $I_{max} = 9$ mA, which is lower than I_{max} at cryogenic temperature. The current of maximal amplitude of oscillations I_{max} decreases as temperature increases [Fig. 2.6(c)]. The decrease in current at elevated temperatures is possibly caused by temperature dependence of spin current generation in Pt. Also the strong temperature dependence of proximity magnetism in Pt due to exchange coupling may affect spectral properties of magnetic layer [59].

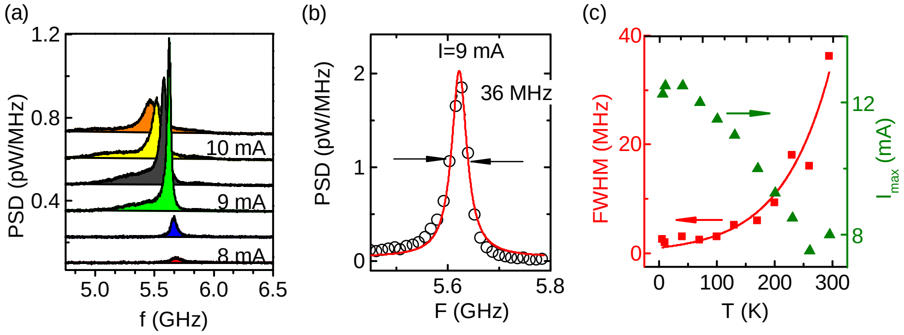

Figure 2.6: Dependence of spectral properties for the device with $d = 400$ nm on temperature. (a) Room-temperature spectra for different currents. (b) Spectrum with maximal amplitude obtained at $I = 9$ mA (Symbols) and fitted with Lorentzian form (Solid line). (c) Dependence of I_{max} (green triangles) and FWHM (red squares) on temperature. Solid line is the exponential fit of data. Reproduced from [7], with the permission of AIP Publishing.

The efficient generation of microwave signal in the devices with nanopatterned Pt layer indicates that not only geometrical localization of current increases spin injection, but also the Pt/FM interface modifies dymanical properties of FM. In devices with nanopatterned Pt spin injector area of Pt/FM interface is small and comparable with the size of localized dynamical mode. Therefore localized spin injector excite localized mode more efficiently than extended proparating mode. To test effect of Pt/Py interface on dymanical properties an additional sample with patterned spin injector and thin 1 nm layer of Pt under top electrodes was fabricated. Because conductivity of the top electrodes is much higher than conductivity of thin Pt spacer under them, negligible amount of current flows through Pt spacer producing spin injection not strong enough to have any effect on dynamics in Py. The spin injection is entirely confined in the region of 400 nm Pt in the gap of electrodes.

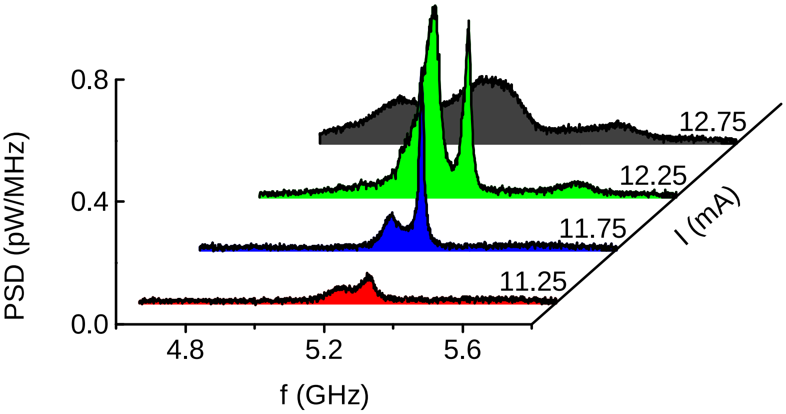

Figure 2.7: Spectra for device with $d = 400$ nm Pt disk and 1 nm Pt under top contacts at room temperature. Reproduced from [7], with the permission of AIP Publishing.

This device demonstrates microwave generation from 6 K to room temperature similar to device with Pt space. However, the spectrum has two distinct peaks at the onset of oscillation at $I = 11.25$ mA [Fig. 2.7]. As the current increases additional high frequency peak appears. This results indicates that Pt/Py interface changes dynamical properties of active FM layer.

It is known that Pt/Py interface increases dynamical damping in FM due to enhanced SO interaction at the interface [56]. However, increased dynamical damping leads only to faster decay of propagating spin wave, and not directly responsibly for multi modal dynamics. Other possible explanation of observed effects inhomogeneous magnetic anisotropy induces by Pt. Spin wave reflection from these inhomogeneities reduces radiative efficiency of high frequency spin wave away from active area of the device cause low coherence of oscillation and microwave generation [58].

2.1.2 Nanoconstriction based SHNO

One of the most important characteristics of microwave oscillators is its ability to generate coherent oscillations. SHNO devices can generated large single mode signal at cryogenic temperatures and/or relatively low electrical current. However, at elevated temperature and/or high current additional dynamical modes are excited. Multi modal dynamics decreases coherency of auto oscillations, reducing efficiency of microwave generation by SHNO. De-coherence can be avoided by selective enhancement of one mode by controlling geometry of auto oscillation region. Coherent microwave generation in a wide range of temperatures can be achieved by utilizing dipolar field to create potential well confinement for the localized auto-oscillation mode.

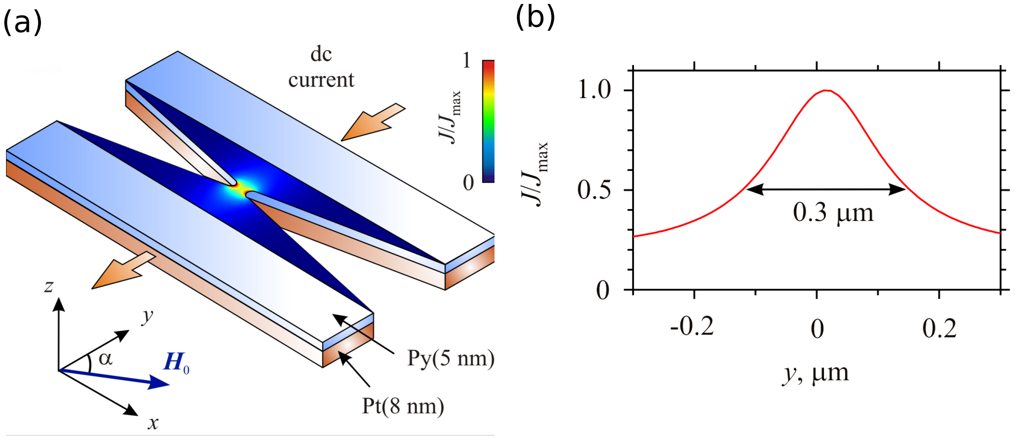

Figure 2.8: (a) Schematic of experimental dives with bow-shape nanoconstriction region with calculated current density map. (b) Calculated current density along Y-axis in the central part of the device for current $I = 1$ mA. Reproduced from [7], with the permission of AIP Publishing.

The schematic of experimental device is shown in Fig. 2.8(a). The device consists of Py(5)Pt(8) bilayer strip of 4 μm wide deposited in high vacuum by magnetron sputtering. In the central area of the strip bow-shape nanoconstriction with an opening angle of 22° was created by Ar ion milling all way through the entire thickness of Py/Pt bilayer. The width of nanoconstriction was 150 nm with 50 nm apex radius. Electrical current flowing through the device has maximal density in nanoconstriction. Figure 2.8(b) shows current density distribution along the device axis Y in Pt layer, calculated independently measured parameters: material resistivity $\rho_{Pt} = 11.2 \pm 0.06\ \mu\Omega\cdot$ cm, $\rho_{Py} = 32.6 \pm 0.06 \mu\Omega\cdot$ cm and current $I = 1$ mA. Due to lower resistivity of Pt layer over than 80% of current flows in Pt. Moreover in nanoconstriction current has a peak of 300 nm width of increased density. Because device operation relies on SHE, high current density in nanoconstriction in Pt leads to strong spin current generation. The region of high current density also defines active area of the device, where injected spin current excite oscillation of magnetization.

To enable efficient electronic microwave generation based on AMR effect external magnetic field H_0 was applied in-plane at the angle $\alpha = 60^{circ}$ to the direction of current. Electronic spectral properties of the SHNO with nanoconstriction is shown in Fig. 2.9. Spin current generated in Pt decreases effective damping in Py due to STT. The damping is completely compensated by STT near critical current I_c, resulting in onset of auto-oscillation. For current device microwave oscillation peak appears around $I_c \approx 3.3$ mA and gradually increasing with increasing current [Fig. 2.9(a)]. Initially spectral line-width decreases with increasing current [Fig. 2.9(c)] and reaches its minimum of 6.2 MHz and maximal amplitude at 3.74 mA [Fig. 2.9(b)]. Integral intensity of microwave signal reaches its maximum of 7 pW at 3.95 mA [Fig. 2.9(c)]. Further increase of

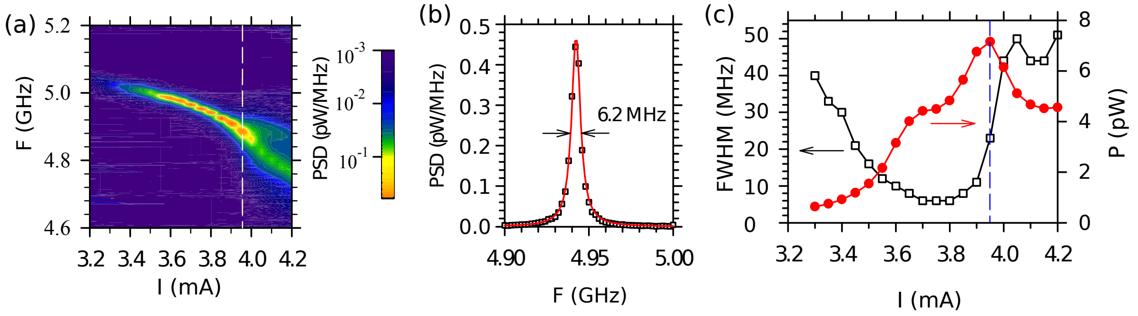

Figure 2.9: Spectral characteristic of nanoconstriction based SHNO at RT obtain with electronic microwave measurements. (a) Map of PSD of microwave signal generated by SHNO in current-frequency coordinates (Logarithmic scale). (b) Spectral peak obtain at $I = 3.75$ mA (symbols) and fitted with Lorentzian shape (solid line). (c) Linewidth and integral power of auto- oscillations vs current. Dashed line shows current at above which system transitions to multi-modal dynamics. Reproduced from [8], with the permission of AIP Publishing.

current leads to spectral broadening of the spectral peak and the it spits in two peaks, indicating transition to multi modal dynamics. Despite relatively low critical current compared with other types of SHNO devices [5,7,53] current density in nanoconstriction comparable to other spin torque devices [15].

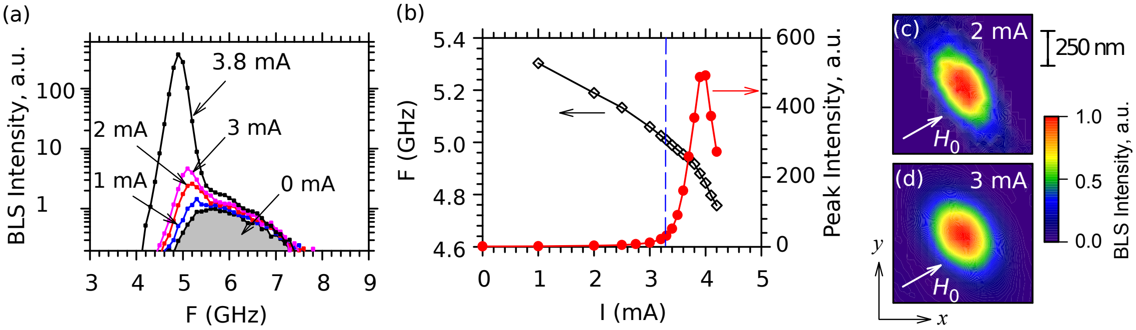

Figure 2.10: Spectral characteristic of nanoconstriction based SHNO at RT obtain with μ-BLS at $H_0 = 400$ Oe. (a) Spectra of magnetization oscillation for different applied current as labeled. (b) Dependence of central oscillation frequency (opened symbols) and peak intensity (solid symbols) on current. (c) Spacial map of intensity of magnetization oscillation obtained at $I = 2$ mA. (d) Same as (c) but at at $I = 3.8$ mA. Reproduced from [8], with the permission of AIP Publishing.

To determine spacial distribution of oscillation the current induced dynamics were detected with μ-BLS technique. The power of probing laser was 0.1 pW, which is low enough to not perturb electronic spectra. Figure 2.10(a) shows spectra of oscillation at different currents. Sensitivity of BLS technique allows to detect thermal fluctuations, spectra of which corresponds to $I = 0$. For currents $I > 0$ the fluctuations are enhanced and additional peak appears at low frequency shoulder of thermal fluctuations. At the onset of auto-osculations for $I > I_c$ peak rapidly increase in intensity. In contrast to self-localized "bullet" mode onset of auto-oscillations of which abruptly appear at I_c [54], in SHNO with nanoconstriction gradually emerges even at $I < I_c$ [Fig. 2.10(b)].

Spacial resolved measurements were performed to elucidate nature of oscillation mode. The active area 1 μm by 1 μm around nanoconstriction was scanned by probing laser focused to its diffraction with a step size of 50 nm at current below [Fig. 2.10(c)] and above [Fig. 2.10(d)] critical. There is no significant difference between oscillation volume for currents below and above critical.

The oscillation area is elongated in the direction perpendicular to external field H_0. The size of oscillation area is approximately 250 by 400 nm, which is larger than typical oscillation area 70 nm of bullet mode [5,54,60]. Large area of oscillations leads to narrow line width of a spectrum, which is confirmed by electronics measurement above.

The micromagnetic simulation (OOMMF package [61]) was used to clarify the nature of auto-oscillation mode as well as effect of dipolar and Oersted field. Figure 2.11(a) shows calculated distribution of demagnetizing field in the area of nanoconstriction. The edges of nanoconstriction produce strong demagnetizing field, which is opposite to static magnetic field reducing internal field in nanoconstriction area.

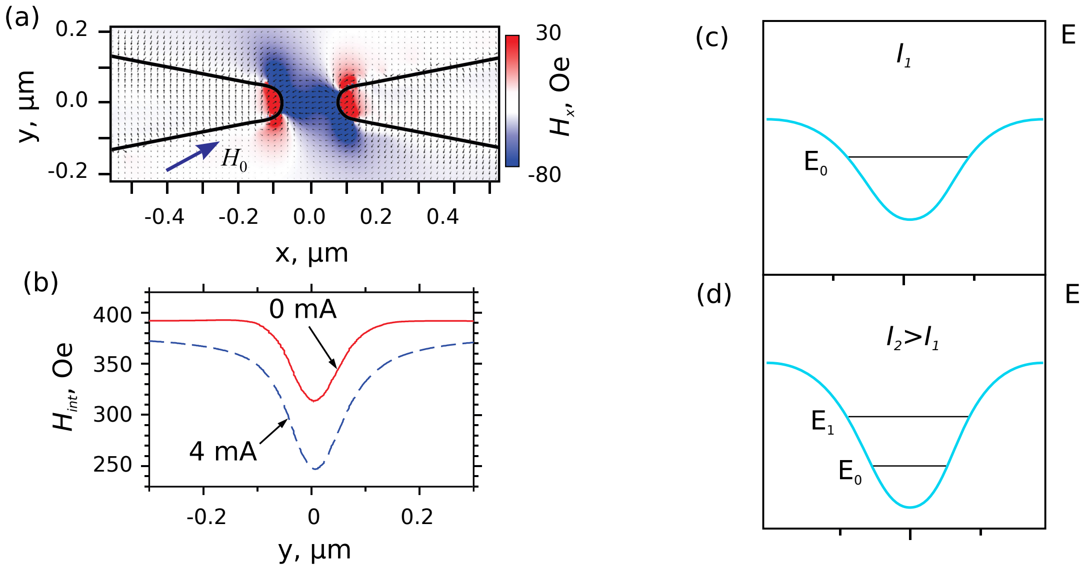

Figure 2.11: (a) Calculated distribution of magnetic field in the area of nanoconstriction in Py. (b) Profile of static magnetic field distribution along the device axis for $I = 0$ (solid line) and $I = 4$ mA (dashed line). (c) Schematic of shallow potential well with one state. (d) Schematic of deep potential well with two states. Reproduced from [8], with the permission of AIP Publishing.

When no current flowing through nanoconstriction demagnetizing field reduces static magnetic field by 80 Oe as shown in Fig. 2.11 (b) solid line. Electrical current generated additional Oersted field which reduces internal effective field even more Fig. 2.11 (b) dashed line. Effective magnetic field creates potential well, which localize single oscillation mode. Oersted field generated by current flowing in positive direction increases depth of potential well. When potential well is deep enough, is has two energy level corresponds to two different frequencies of oscillation. This can explain, that spectral peak spits into two at higher current [Fig. 2.10(a)].

Chapter 3

Synchronization of SHNO

3.1 Synchronization of SHNO to external signals [1]

With the experimental demonstration of the generation of pure spin currents — directional flows of angular momentum not tied to the flow of electrical charge — the development of spin-based electronic (spintronic) devices has entered a new phase [62, 63]. It has now become possible to exploit a range of both electrically conducting and insulating magnetic materials that would be incompatible with conventional magnetic multilayer structures using spin-polarized charge currents. Moreover, planar device geometries operating via spin currents generated by the SHE are generally scalable, enabling us to envision the operation of devices with dimensions ranging from nanometers to millimeters [34, 35, 53, 58, 64–66].

Following the pioneering work demonstrating the possibility of reducing effective magnetic damping using spin currents generated by SHE [64], complete compensation of damping has recently been realized in magnetic nanostructures [5, 35, 53]. The resulting spontaneous microwave-frequency oscillations can be utilized for the generation of signals for next-generation integrated electronics.

---

[1] Published article: V.E. Demidov, H. Ulrichs, S.V. Gurevich, S.O. Demokritov, V.S. Tiberkevich, A.N. Slavin, A. Zholud S. Urazhdin, "Synchronization of spin Hall nano-oscillators to external microwave signals". Nat. Comm. 5, 3179 (2014).

Spin-torque nano-oscillators (STNOs) driven by SHE – spin Hall nano-oscillators (SHNOs) – have several advantages over conventional STNOs. In particular, pure spin currents are less likely to cause damage by electromigration or by Ohmic heating in the ferromagnets. Additionally, their geometry facilitates direct optical access to the active device area enabling unprecedented measurements by advanced magneto-optical techniques and thus elucidating the dynamic phenomena induced by spin currents [5, 58].

One of the distinguishing characteristics of STNOs is a strong nonlinearity which enables their efficient synchronization to external periodic signals over a wide frequency range [67–70]. This synchronization may allow the development of microwave sources with improved generation coherence using mutually synchronized STNO arrays. The implementation of such arrays with SHNOs is significantly more straightforward than with conventional STNOs due to their more simple, planar geometry. However, synchronization of SHNOs to microwave signals has yet to be demonstrated. Here, it was reported an experimental study of the response of SHNOs to external microwave signals. It was demonstrated that SHNOs exhibit efficient parametric synchronization when the external driving frequency is close to twice their oscillation frequency, with a relatively wide synchronization frequency interval controlled by the magnitude of the microwave signal and by the dc current flowing through the device. In contrast with the synchronization of conventional STNOs based on giant magnetoresistive structures [69,70], the synchronization of SHNOs occurs only above a certain threshold external microwave signal power. The analysis shows that synchronization is suppressed below the threshold through the influence of spin wave modes enhanced by the spin current.

3.2 Results

The test devices are formed from a bilayer comprising a 8 nm thick film of Pt and a 5 nm thick film of Permalloy (Py) patterned into a disk with the diameter of4μ m [Fig. 3.1(a)]. Two 150 nm thick Au electrodes placed on top of the bilayer form an in-plane point contact. The endpoints of the Au electrodes have a 50 nm radius and are separated by a 100 nm wide gap. To induce oscillations

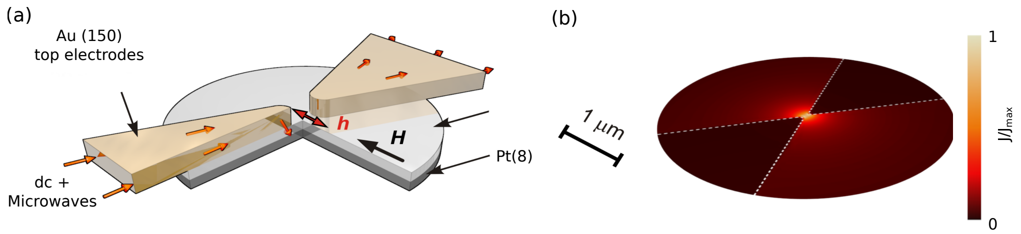

Figure 3.1: Experimental configuration. (a) Schematic of the test device. (b) Normalized calculated distribution on the driving current density in the device plane. Adopted from Ref. [9].

of the Py magnetization, a dc current I is applied between the Au electrodes. Calculations of the current distribution based on a three-dimensional model of the device show that, because of the large difference between the sheet resistances of the electrodes and the Py/Pt bilayer, the current is concentrated predominantly in the gap between the electrodes within an area with a characteristic size of about 250 nm [Fig. 3.1(b)].

The electric current flowing in the Pt layer produces, via the spin Hall effect, a pure spin current directed perpendicular to the bilayer plane [32, 71]. This spin current exerts a spin-transfer torque on the magnetization of the Py which results in a modification of its dynamic magnetic damping [64], and an enhancement (or suppression) of thermal magnetization fluctuations [58] depending on the direction of the electric current relative to the magnetic field $\mathbf{H}$. In the studied geometry, positive current as defined in Fig. 3.1(a) results in reduction of the effective damping. The magnetization of Py starts to auto-oscillate when the dynamic damping is completely compensated. The magnetization dynamics in the Py layer was detected by micro-focus BLS [52]. The BLS intensity at a given frequency is proportional to the intensity of magnetization oscillations at this frequency at the position of the probing laser spot, which in our experiment was centered in the gap between the electrodes.

Figure 3.2 illustrates the evolution of the BLS spectra under the influence of current I, at $H = 800$ Oe. A broad peak observed at $I < 16$ mA is caused by thermal magnetization fluctuations enhanced by the spin current, as illustrated for $I = 10$ mA and $I = 15$ mA in Figs. 3.2(a) and (b), respectively. A narrow peak with a center frequency of about 7 GHz appears below

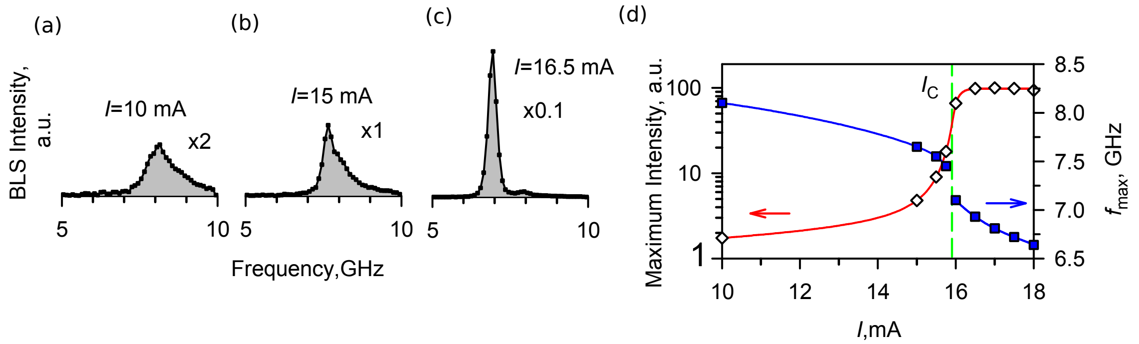

Figure 3.2: Evolution of the spectra under the influence of current. (a) - (c) Magnetization oscillation spectra recorded at the labelled values. (d) Maximum BLS (open symbols) and the corresponding frequencies (solid symbols) versus current, at $H = 800$ Oe. Lines are guides for the eye. The data were obtained by BLS. Adopted from Ref. [9].

the thermal fluctuation peak in the range $15.75 < I < 16$ mA (metastable auto-oscillation regime) and quickly increases in amplitude starting to dominate over the broad fluctuation peak already at $I = 16$ mA [Fig. 3.2(c)]. We identify this current value with the critical current I_C, at which the dynamical damping is completely compensated by the spin transfer torque exerted by the pure spin current, resulting in the onset of auto-oscillation. The maximum detected BLS intensity gradually increases with increasing $I < I_C$, abruptly jumps at $I = I_C$, and then saturates at $I > 16.5$ mA [Fig. 3.2(d), note the logarithmic scale on the vertical axis]. The frequency f_{max} corresponding to the maximum of the BLS intensity gradually decreases with increasing $I < I_C$ due to the nonlinear frequency shift associated with the enhancement of thermal magnetization fluctuations, and then drops abruptly at $I = I_C$ [Fig. 3.2(d)]. This abrupt decrease clearly marks the onset of auto-oscillations via the formation of a nonlinear self-localized spin-wave "bullet" mode at frequency below the linear spectrum of propagating spin waves. The transition to the auto-oscillation regime is observed only at $I > 0$, while at $I < 0$ thermal magnetization fluctuations are increasingly suppressed and no auto-oscillation is observed. Rotation of the static field by 180° results in the inversion of these effects with respect to the direction of I, in agreement with the symmetry of the spin Hall effect.

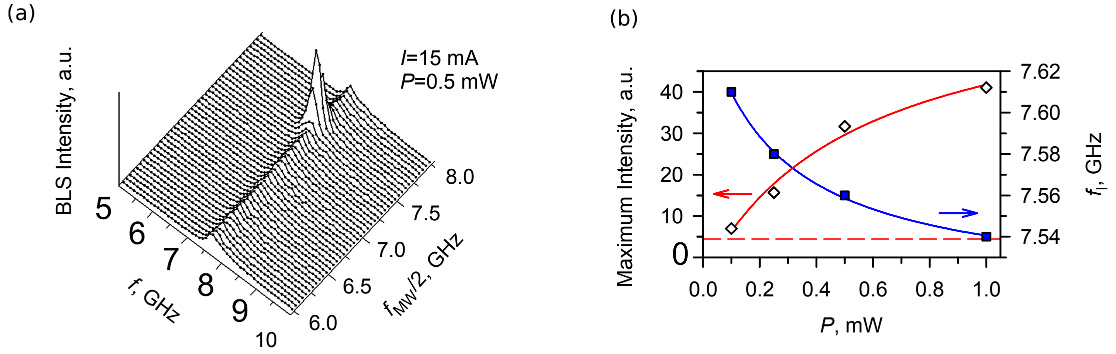

Figure 3.3: Effects of the microwave signal below the onset of autooscillation. (a) BLS spectra recorded at $I = 15$ mA, with the frequency f_{MW} of the microwave varying from 12 to 16 GHz in 0.1 GHz increments. The power of the signal is $P = 0.5$ mA. (b) Maximum intensity of the BLS spectrum (open symbols) and the corresponding frequency f_i (solid symbols) versus driving microwave signal P. Solid lines are guides for the eye. Dashed line shows the maximum intensity in the absence of the microwave signal. Adopted from Ref. [9].

3.3 Effect of the external microwave signals

To study the effects of external signals on the oscillation characteristics of the SHNOs, a bias tee was used to apply a microwave current at frequency f_{MW} simultaneously with the dc current I. The microwave current induces in the Py film an additional dynamic magnetic field h collinear with the static field $\mathbf{H}$ [Fig. 3.2(a)]. The maximum power of the applied microwave signal was $P = 2$ mW, which corresponds to a dynamic field $h \approx 57$ Oe, while the spatial distribution of $\mathbf{h}$ was found to be very close to that of the current density [Fig. 3.2(b)]. In the $\mathbf{h}||\mathbf{H}$ geometry, the dynamic magnetic field couples to the dynamic magnetization through a parametric process that becomes efficient when the driving frequency is close to twice the auto-oscillation frequency [72, 73]. Therefore, the response of the SHNOs to microwave signals having frequencies close to 14 GHz was measured below. Note that by rotating the direction of field $\mathbf{H}$ away from the direction perpendicular to the current flow, one can, in principle, also achieve direct linear coupling of magnetization to external microwaves at the fundamental frequency. However, due to the symmetry of the spin-Hall effect, such rotation results in a dramatic increase of the critical current I_C, which makes the operation of SHNO inefficient.

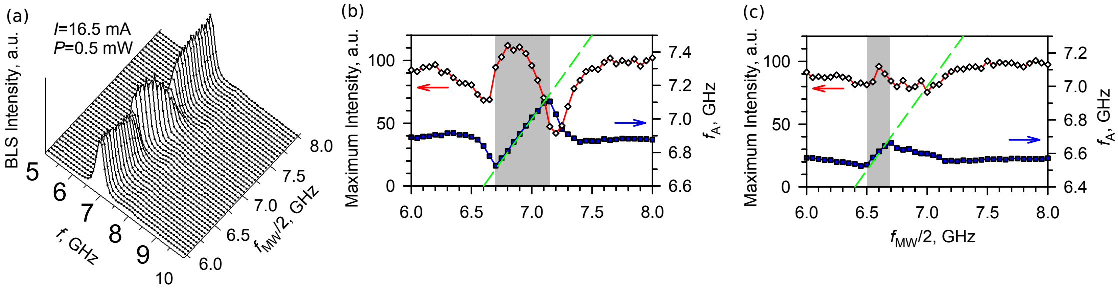

Figure 3.4: Effect of microwave signal above the onset of autooscillation. (a) BLS spectra recorded at $I = 16.5$ mA, with the frequency f_{MW} of the microwave signal varying from 12 to 16 GHz with increments 0.1 GHz. The power of the signal $P = 0.5$ mW. (b) Maximum intensity of the BLS spectrum (open symbols) and the corresponding autooscillation frequency f_A (solid symbols) versus driving microwave frequency. Shaded area marks the synchronization interval. Dashed line shows the dependence $f_A = f_{MW}/2$. (c) Same as (b), for $I = 18$ mA. Adopted from Ref. [9].

First, the effects of the microwave signal at dc currents below the onset of auto-oscillation was analyzed, as illustrated in Fig. 3.3(a) for $I = 15$ mA and f_{MW} varying from 12 to 16 GHz. The effect is significant only over a narrow frequency interval, when $f_{MW}/2$ is close to the ferromagnetic resonance (FMR) frequency of the Py film. A strong increase of the BLS intensity within this interval is caused by parametric spin-wave instability induced by the microwave signal.

To quantify the parametric instability, the frequency f_I at which the peak BLS intensity reaches a maximum was determined, at a given excitation power P. Figure 3.3(b) shows that f_I monotonically decreases with increasing P, due to nonlinear frequency shift, while the corresponding maximum peak intensity exhibits a monotonic increase, gradually saturating at large P. The maximum intensity exceeds the thermal level, shown with a horizontal dashed line, only at driving powers above the threshold value $P^P_{th} \approx 0.07$ mW, in agreement with the theory of the parametric instability.

Next, the effects of the external microwave signal in the auto-oscillation regime of the SHNOs was studied, at $I > I_C$. Figure 3.4(a) shows the data obtained for $I = 16.5$ mA, where the amplitude of the auto-oscillations saturates [Fig. 3.2(d)] marking the stable auto-oscillation regime of SHNO. In contrast with the subcritical regime, the BLS spectra exhibit a narrow intense auto-

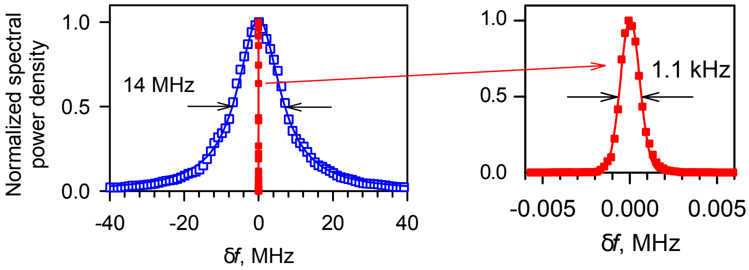

Figure 3.5: . Electronic characterization of the auto-oscillation linewidth. Spectra of SHNO auto-oscillations obtained for the free-running oscillation without external microwave signal (open symbols) and oscillation synchronized with the external microwave signal (solid symbols). Inset shows the synchronized spectrum on a finer frequency scale. δf denotes detuning from $f_{MW}/2$. Curves show the result of the fitting of the experimental data by the Lorentzian function for the free-running spectrum, and Gaussian for the synchronized spectrum. Adopted from Ref. [9].

oscillation peak, regardless of the external microwave frequency [Fig. 3.4(a)]. When $f_{MW}/2$ approaches the auto-oscillation frequency, the latter starts to exactly follow $f_{MW}/2$ [solid symbols in Fig. 3.4(b)], as expected for parametrically synchronized oscillation, and as previously observed for conventional STNOs. However, unlike in conventional STNOs, where a large increase of intensity is observed in the synchronized regime, the intensity of oscillation of the SHNOs varies only slightly throughout the external frequency range, with the largest intensity near the middle of the synchronization interval, and two minima near the synchronization limits (open symbols in Fig. 3.4(b)). With the increase of the driving current [Fig. 3.4(c)] the above behaviors are generally preserved, although the width of the synchronization interval noticeably reduces.

Although the BLS measurements clearly demonstrate the frequency locking of the studied SHNOs to the external microwave signal, observation of the behavior of the auto-oscillation linewidth is highly desirable to obtain unambiguous evidence of the synchronization. Since the limited frequency resolution of the BLS technique does not allow to obtain this information, additional electronic measurements were performed. These measurements demonstrate that in the range of frequencies, where the frequency locking is observed, the linewidth of the auto-oscillation reduces by more than four orders of magnitude [Fig. 3.5], as one expects for the synchronized

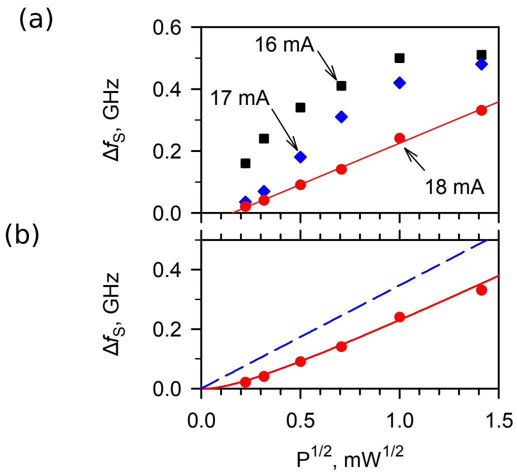

Figure 3.6: Dependence of the synchronization interval on the dynamic field. (a) Measured synchronization interval versus $P^{1/2}$, at the labelled values of dc current I. Solid line is a linear fit of the $I = 18$ mA data. (b) Symbols: measured synchronization interval versus $P^{1/2}$, at $I = 18$ mA.Solid curve: calculated synchronization interval in the presence of noise.Dashed curve is the same dependence calculated in the absence of noise. The experimental data were obtained by BLS. Adopted from Ref. [9].

regime.

To gain further insight into the synchronization process, it is necessary to measure the dependence of the synchronization interval Δf_S on the dynamic microwave magnetic field $\mathbf{h}$, which is proportional to the square root of the driving microwave power P. The dependencies of Δf_S on $P^{1/2}$ obtained at different values of dc current are shown by the symbols in Fig. 3.6(a). No synchronization was observed at microwave powers below $P_{th}^S \approx 0.03$ mW, regardless of the dc current value. At a current $I = 18$ mA significantly above the oscillation onset, Δf_S exhibits an approximately linear dependence on $P^{1/2}$ above the threshold [circles and solid straight line in Fig. 3.6 (a)], while at smaller currents close to the oscillation onset, a rapid increase of Δf_S at small microwave power is followed by saturation [squares and diamonds in Fig. 3.6(a)]. The observed behaviors are not described by the theory of synchronization of nonlinear single-mode oscillators, which predicts a universally linear dependence of Δf_S on $P^{1/2}$. The predicted dependence also starts at the origin, since the synchronization is known to be a non-threshold phenomenon.

3.4 Discussion

Now it is necessary to show that the synchronization threshold observed can be explained by the effects of thermal noise enhanced by the spin current on the self-localized "bullet" oscillation mode. The analysis is based on the theory of auto-oscillator synchronization developed in Ref. [74], applying it to the "bullet" oscillation mode of the SHNOs, and taking into account analytically the effect of thermal noise that was introduced numerically in Ref. [68]. The spin-wave "bullet" can be described by a perturbed nonlinear two-dimensional Schrödinger equation [54]:

$$\frac{\partial a}{\partial t} + i(2\pi f_0 - D\Delta^2 + N|a|^2)a = F(a,t) \tag{3.4.1}$$

where $a = |a|exp[i\Psi(t)]$is the complex amplitude of the "bullet" mode, f_0 is the ferromagnetic resonance frequency, D is the spin-wave dispersion coefficient, and N is the nonlinear frequency shift coefficient. The term $F(a,t) = F_d(a,t) + S_n(t)$ on the right-hand side of Eq. (3.4.3) comprises a deterministic term $F_d(a,t)$ and a stochastic term $S_n(t)$. The former accounts for the Gilbert damping, the negative damping produced by the spin current via the spin torque mechanism, and for the Zeeman torque exerted by the external microwave signal. The stochastic term $S_n(t)$ describes the effect of thermal noise. For a well-developed spin-wave "bullet" (dc current sufficiently above I_C) the effects of perturbations can be analyzed in the framework of modulation theory [75]. To describe the synchronization process in the framework of this theory it is convenient to renormalize oscillation phase $\Delta\Phi = 2\Psi(t) + 2\pi f_{MW} t + \Delta\Phi$, where $\Delta\Phi$ is a nonlinear phase shift that accounts for the dependence $f_g(a)$ of the generation frequency f_g on the auto-oscillation amplitude a. Then, the evolution equation for the renormalized phase is

$$\frac{\mathrm{d}\Phi}{\mathrm{d}t} = 4\pi\Delta f_{MW} - 2\pi\Delta f_0 \sin\Phi + \sqrt{\mu} s_n(t) \tag{3.4.2}$$

where $\Delta f_{MW} = f_g - f_{MW}/2$, and Δf_0 is the synchronization interval in the absence of noise, which is proportional to the amplitude h of the microwave signal, $s_n(t)$ is the normalized thermal white noise characterized by auto-correlation $< s_n(t)s_n^*(t') >= \delta(t-t')$, and $\mu = (1+\nu^2)\Gamma(k_B T/E)$is the amplitude of thermal noise measured in units of angular frequency and numerically equal to the generation linewidth of the free-running auto-oscillator. Here ν is the nonlinearity coefficient, Γ is the Gilbert damping rate, k_B is the Boltzmann constant, T is temperature, and E is the energy of the "bullet" mode that can be found using Eq. (77) in Ref. [74] and Eqs. (6), (7) and (10) in Ref. [54].

Using the standard Fokker-Planck formalism [76], the stochastic Eq. (3.4.2) can be transformed into a deterministic Fokker-Planck-type equation for the probability distribution of the normalized phase. The solution of this equation gives an explicit expression for the frequency of the perturbed "bullet" in the presence of noise

$$f_A = f_{MW}/2 - \mu\Big(\int_0^{2\pi} e^{u(\Phi)}\Big(C + \int_0^{\Phi} e^{-u(\Phi)} d\Phi'\Big) d\Phi\Big)^{-1} \tag{3.4.3}$$

where $C = -(1 - e^{-8\pi^2 \Delta f_{MW}/\mu})^{-1} \int_0^{2\pi} e^{-u(\Phi')} d\Phi'$ and $u(\Phi) = (4\pi\Delta f_{MW} + 2\pi\Delta f_0 \cos\Phi)/\mu$. Equation (3.4.3) is the analytical solution of the synchronization problem in the presence of noise, which allows one to directly calculate the dependence of the synchronization interval ΔF_S on the microwave power P. It is reduced to Eq. (55) in Ref. [74] in the limit of negligible noise $\mu \to 0$.

The solid curve in Fig. 3.6(b) shows the result of the calculation for $I = 18$ mA using $\mu/2\pi = 46$ MHz and $\Delta f_0 = BP^{1/2}$ with $B = 350$ MHz/(mW)$^{1/2}$ as the only fitting parameters. The inclusion of the effects of noise in the model results in a decrease of the synchronization interval Δf_S and a non-zero apparent power threshold of the synchronization process. By contrast, the same calculation neglecting the effects of noise [dashed curve in Fig. 3.6(b)] yields no threshold for synchronization, in qualitative disagreement with the data.

The effective noise amplitude μ at room temperature can be calculated from Eq. (3.4.3) with a value $\nu \approx 2$ typical for the in-plane magnetized film, giving $\mu/2\pi \approx 0.4$ MHz, which is significantly smaller than the value $\mu/2\pi = 46$ MHz obtained by fitting the experimental data. The discrepancy between these values can be attributed to the effect of the spin current on the magnetic noise in the SHNOs: the dynamic magnetic modes are pumped to well above their thermal levels by the spin current and accordingly the effective temperature of the magnetic system corresponding to the low-energy fluctuations significantly exceeds that of the lattice, resulting in a large apparent threshold for synchronization [Fig. 3.6]. To verify this hypothesis it is necessary to perform additional measurements at low temperature of the lattice that the reduction of the lattice temperature does not result in the reduction of the synchronization threshold.

Note that the suggested theory is incapable of quantitatively describing the dependence of Δf_S on $P^{1/2}$ obtained at dc currents close to I_C [see $I = 16$ mA and $I = 17$ mA data in Fig. 3.6(a)]. Two mechanisms responsible for this disagreement can be identified. Firstly, the mode rigidity assumption underlying the analysis does not hold for small oscillation amplitudes, since external perturbations can make a significant contribution to the energy balance of the "bullet" mode. Secondly, the approximation of uncorrelated white noise is not valid in this regime as the non-equilibrium populations of magnetic modes deviate significantly from the thermal distribution in the vicinity of the damping compensation point. On the other hand, at larger currents one can expect that stronger nonlinear effects result in more efficient thermalization of spin waves.

Chapter 4

Prediction of quantum spin transfer

4.1 Limitation of semi-classical spin transfer model

Spin transfer [36, 77] – the transfer of angular momentum from spin-polarized electrical current to magnetic materials – has been extensively researched as an efficient mechanism for the electronic manipulation of the static and dynamic states in nanomagnetic systems, advancing the understanding of nanomagnetism and electronic transport, and enabling the development of energy-efficient magnetic nanodevices [15,37–39,78–85]. The present understanding of spin transfer is based on the classical approximation for the magnetization, even though the spin-polarized electrons mediating spin transfer are treated quantum-mechanically [42].

The original theoretical models and the interpretations of the experimentally observed effects of ST on magnetization were often based on the simplified approximations that neglected all the dynamical states of FM except for the uniform precession, or equivalently FMR mode, or some other dynamical mode that was singled out based on the geometry of the ST structure [36,38,39,77]. However, subsequent theoretical analysis [54], micromagnetic simulations [80,86], and experimental observations [87–90], demonstrated the complexity of the dynamical states induced by ST [58]. In particular, it was shown that the whole spectrum of the dynamical magnetic modes — the spin waves (or their quanta, magnons) — are involved in ST-induced magnetization dynamics. In this context, it is useful to outline the important general properties of magnons. At typical fields **H** in the kOe range, the magnon spectrum extends from the frequencies of a few GHz (10 $\approx$ V energy scale) to THz (100 meV scale). The dispersion is approximately parabolic $E \approx Dk^2$, where E is the magnon energy, D is the exchange stiffness, and k is the wavevector. The resulting spectral density is proportional to $\sqrt{E}$, i.e. high-frequency magnons dominate the spin-wave spectrum.

ST and damping can be represented in terms of magnons generation and recombination. One can assume that the total spin **S** of FM precesses at an angle Θ relative to its equilibrium orientation opposite to **H**. Since each magnon contributes spin 1 to the projection of **S** on **H**, the number of magnons is

$$n = S(1 - \cos\Theta) \approx S\frac{\Theta^2}{2}. \tag{4.1.1}$$

The damping torque is $\tau_{GL} = -\alpha_{GL}\mu\mathbf{m}\times[\mathbf{m}\times\mathbf{H}] \approx \alpha\mu H\Theta$. Similarly, for spin current polarization along the field, $\tau_F = \hbar J_S\Theta$. Thus, $\hbar S\frac{\mathrm{d}\Theta}{\mathrm{d}t} = \tau_F - \tau_D = (\hbar J_S - \alpha H)\Theta$. Using Eq.(4.1.1), this can be re-written as:

$$\frac{\mathrm{d}n}{\mathrm{d}t} = Bn - \frac{n}{\tau} \tag{4.1.2}$$

where ω is the magnetization precession frequency, $\tau = \hbar\frac{S}{2\alpha\mu H} = \frac{1}{2\alpha\omega}$, and $B = 2J_S/S$. Thus, at small Θ the Landau damping is equivalent to the relaxation-time approximation for the magnon population, and ST can be interpreted as the stimulated emission of magnons driven by the spin current injection [91]. The form Eq. (4.1.2) is easily extended to finite temperature T, by replacing the last term with $\frac{n-n_0}{\tau}$. Here, $n_0 = \frac{1}{Exp(\hbar\omega/kT)-1}$ is the average number of magnons in this mode in thermal equilibrium. In the stationary state, $\frac{\mathrm{d}n}{\mathrm{d}t} = 0$:

$$n(J_S) = \frac{n_0}{1 - \frac{J_S}{J_{S,C}}} \tag{4.1.3}$$

where $J_{S,C} = S/2\tau$ is the critical spin current, at which $n \to \infty$. The validity of Eq. (4.1.3) was confirmed by direct magneto-optical measurements of magnon population vs J_S [5, 58].

The angular momentum conservation argument underlying the existing ST theories has been successful in predicting and explaining a multitude of experimental observations. However, this argument may not uniquely define the outcome of spin flow across magnetic interfaces, and therefore additional, in some cases significant or even dominant contributions to ST may exist. Two outcomes are possible for the scattering of the conduction electron with the opposite spin orientation: spin-up or spin-down. Both are consistent with the angular momentum conservation, and their relative probabilities are determined by the interaction between the electrons.

In particular, if the effect of exchange interaction between the electrons is sufficiently large ($tE_{ex} > h$, where t is the interaction time, h is the Planck's constant, and E_{ex} is the exchange energy), the probabilities of these outcomes are equal, i.e. the conduction electron spin-flips with a 50% probability. The described effect represents a type of ST, i.e. it involves angular momentum transfer between the transport electrons and the nanomagnetic system formed by a single electron spin. However, this ST mechanism does not involve any angular momentum component noncollinear with the "magnetization", and therefore it is not captured by the Slonczewski's theory.

Analysis presented below shows that ST due to quantum fluctuations (quantum ST) becomes dominant when quantum fluctuations of magnetization become comparable to thermal fluctuations, i.e. $\hbar\omega \sim kT$. Since the average magnon energy is $\epsilon > 1$ meV in typical FM, and the entire magnon spectrum is involved in ST, one can expect that quantum ST becomes dominant at T below a few dozen Kelvins. Since magnons with large energies are involved in ST, one can expect additional effects to come into play. First, energy conservation may impose limitations on the dynamical states induced by the spin current. This was first suggested by Tsoi et al. [78] based on the abrupt onset of current-induced magnetization dynamics. However, it was later shown that the onset is determined by the compensation of the effective dynamical damping described by Slonczewski's theory [36]. The energy of magnons is neglected in the Slonczewski's model, since $\mathbf{M}$ is assumed stationary over the duration of the conduction electron's interaction with FM (adiabatic approximation). Since the frequency of the electron's spin precession in FM is similar to that of meV-range magnons involved in ST, one can expect that the interplay between the two dynamics, or equivalently the energy conservation, can result in selective excitation of only certain magnon modes by ST. This effect may be particularly useful for applications of ST in current-driven magnetization reversal (in magnetic memory) and precession (in microwave generation), since it may be possible to tailor the magnetic and geometric properties of nanodevices to enhance or suppress these resonant effects.

4.2 Quantum model of spin transfer

Proposed model for the effects of spin transfer incorporating the quantum magnetization fluctuations builds on the ideas of Berger [77], who was first to describe spin transfer in terms of the spontaneous emission and stimulated emission and absorption of magnons. The spontaneous emission introduced, but ultimately neglected in Berger's analysis of the low-frequency long-wavelength modes can be equivalently described as the spin transfer due to quantum magnetization fluctuations.

The model proposed here is base on a formulation of the problem of current-induced phenomena in the magnetic nanopillars as that of a single scattering event between a spin-polarized electron by a single magnetic layer. This approach allows to avoid the complications associated with the spin-diffusion in the magnetic multilayer, non-essential for the understanding of the demonstrated quantum effects. Next step is to analyze the effects of scattering on the ferromagnetic resonance (FMR) dynamical mode of the magnetization. First it is necessary to determine the outcome of scattering for a single electron, and then extend the analysis to the stationary-state population of the FMR mode. Finally, the analysis is extended to the entire dynamical spectrum of the magnetic nanopillar. Dipolar effects are neglected throughout the analysis. These effects are important for the characteristics of the low-frequency (dipolar) dynamical modes, but have little effect on the high-frequency (exchange) modes which dominate the described phenomena due to their large phase volume.

The proposed model is based on the model of Urazhdin [92] in the limit of low current. This model for the magnetic nanopillars allows to describe spin-dependent electron transport in

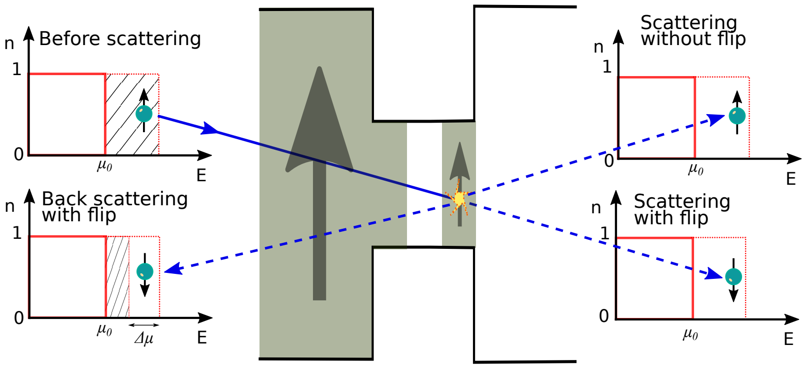

Figure 4.1: Schematic of electron scattering in the magnetic nanopillar. Solid line shows electron's state before scattering. Dashed lines are possible outcomes of scattering.

these structures in terms of scattering of spin-polarized electrons by a single nanomagnet. This Landauer-type model, which is similar in spirit to the spin-circuit theory of Brataas *et al.* [93] is schematically illustrated in Fig. 4.1. The nanopillar forms a nanoconstriction between two large electrodes. One of the electrodes contains the spin-polarizing ferromagnetic layer. A bias applied between the electrodes modifies the relative position of the chemical potentials in the electrodes, as shown schematically in Fig. 4.1 for both electrodes, for $T = 0$. Electron spin-filtering in the polarizer results in the spin-dependence of the chemical potential in the left electrode containing the polarizer. At $I < 0$ corresponding to the electron flow from the polarizer to the free layer, the majority-electron chemical potential in the left electrode is higher than the minority chemical potential, and both are higher than the potential in the right electrode. The difference between the chemical potentials for spin-up and spin-down electrons is related to the spin accumulation in the theory of diffusive spin transport in magnetic multilayers [94].

Figure 4.1 also schematically shows the scattering of an electron which initially moves in the left electrode towards the nanoconstriction. Its initial magnetic moment is up (majority electron), and its energy is larger than the chemical potential in the right electrode. The electron is scattered by the nanomagnet, and is reflected as a minority electron, or transmitted as a spin-up or spin-down electron. The reflection is possible if the energy of the electron is sufficiently high such that there are available states in the left electrode. Assuming that the electron is scattered in the nanopillar only once, and is then absorbed by the large electrodes where the spin-dependent electron distribution is in quasi-equilibrium and is not significantly affected by the scattered electron. In this approximation, the spin-dependent potentials in the electrodes entirely determine the rate of spin-dependent scattering of electrons by the free layer. In this analysis, these rates are described by the parameters I and p, such that $I(1+p)/2e$ is the rate of scattering of the majority electrons, and $I(1-p)/2e$ is the rate of scattering of the minority electrons.

It is necessary to note that I is related to the charge current through the nanopillar but is not identical to it. For example, at finite temperature T, the electron distribution in the electrodes is described by the Fermi-Dirac function, such that the scattering schematically shown in Fig. 4.1 can occur even in the absence of bias current. In the current approach, this can be accounted for by a convolution of the current-dependent scattering derived in the $T = 0$ limit, with a distribution of currents with the width kT, consistent with the experimental observations described in the main text. Similarly, the polarization p describes the spin-filtering properties of the polarizer, related to but not identical to the spin polarization of the current, because the latter is also affected by the spin-dependent transport properties of the free layer.

Electron scattering modifies state of nanomagnet. Initially for simplicity, it is necessary to consider scattering of a single spin-polarized electron described by a spinor $|s\rangle = (a, b) = a|\uparrow\rangle + b|\downarrow\rangle$, by the magnetization of the nanopillar described by a quantum macrospin $|L, L_z\rangle$, where L is the total angular momentum, and L_z is its projection onto the quantization axis aligned opposite to the magnetic field B [92,95]. The interaction between the two spins is described by the standard exchange Hamiltonian $\hat{H}_{ex} = J_{ex}\vec{s}\cdot\vec{L}/L$, where J_{ex} is the Heisenberg exchange constant. The electron's spin is scattered by the magnetic material, described by turning on $\hat{H}_{ex}$, resulting in the precession of both $\vec{s}$ and $\vec{L}$ around the total angular momentum $\vec{J} = \vec{s} + \vec{L}$. The spatial degrees of freedom are not explicitly included in the model: in the macrospin approximation, they affect only the interaction time between the electron and the magnetic layer, resulting in the variations of the precession phases acquired by $\vec{s}$ and $\vec{L}$. The details of these variations are not important in the random-phase approximation discussed below.

To analyze the spin evolution due to the exchange interaction, the state $|L, L_z\rangle \otimes |s\rangle$ need to be expressed in the expanded basis $|J, J_z\rangle$ of the eigenstates of the total angular momentum and its projection on the z-axis. The initial state is

$$\psi_i = a|L, L_z\rangle \otimes |\uparrow\rangle + b|L, L_z\rangle \otimes |\downarrow\rangle \tag{4.2.1}$$

In the expanded basis, the first term in Eq. (4.2.1) is:

$$a : |L, L_z\rangle \otimes |\uparrow\rangle = A_{\uparrow}|L + \frac{1}{2}, L_z + \frac{1}{2}\rangle + B_{\uparrow}|L - \frac{1}{2}, L_z + \frac{1}{2}\rangle \tag{4.2.2}$$

and the second term:

$$b : |L, L_z\rangle \otimes |\downarrow\rangle = A_{\downarrow}|L + \frac{1}{2}, L_z - \frac{1}{2}\rangle + B_{\downarrow}|L - \frac{1}{2}, L_z - \frac{1}{2}\rangle \tag{4.2.3}$$

Here $A_{\uparrow,\downarrow}$ and $B_{\uparrow,\downarrow}$ are the Clebsch-Gordon coefficients. To find these unknown coefficients it is necessary to start by taking inner product of Eq. (4.2.1) with each basis element. In general form it can written the following way ($J = L + S$, $L = J - S$):

$$\langle J, J_Z|L_+|L, L_z\rangle \otimes |\uparrow\rangle = \langle J, J_Z|J_-^* - S_+|L, L_z\rangle \otimes |\uparrow\rangle \tag{4.2.4}$$

After taking into account that $J_+ = J_-^*$ and applying are raising operators to corresponding states (operator L_+ acts in macrospin subspace, operator S_+ acts in single spin subspace) and the following expression is obtained:

$$\begin{gathered}\sqrt{(L - L_z)(L + L_z + 1)}\langle J, J_Z|L, L_z + 1\rangle \otimes |\uparrow\rangle = \\ \sqrt{(J + J_Z)(J - J_Z + 1)}\langle J, J_Z - 1|L, L_z\rangle \otimes |\uparrow\rangle\end{gathered} \tag{4.2.5}$$

Substituting $J = L + 1/2$, $J_Z - 1 = L_z + 1/2$ in the Eq. (4.2.5) one obtains:

$$\langle L + \frac{1}{2}, L_z + \frac{3}{2}|L, L_z + 1\rangle \otimes |\uparrow\rangle = \frac{\sqrt{(L + L_z + 2)}}{\sqrt{(L + L_z + 1)}}\langle L + \frac{1}{2}, L_z + \frac{1}{2}|L, L_z\rangle \otimes |\uparrow\rangle \tag{4.2.6}$$

Scalar products in this equation are numbers $A_{\uparrow L_z}$ and $A_{\uparrow L_z+1}$, so the first recursion retaliation for $A_{\uparrow L_z}$ is:

$$A_{\uparrow L_z+1} = \frac{\sqrt{(L + L_z + 2)}}{\sqrt{(L + L_z + 1)}}A_{\uparrow L_z} \tag{4.2.7}$$

To get recursion for $B_\uparrow$ it is necessary to plug in the following values $J = L - 1/2$ and $J_Z - 1 = L_z + 1/2$ into Eq. (4.2.5):

$$B_{\uparrow L_z+1} = \frac{\sqrt{L - L_z - 1}}{\sqrt{L - L_z}}B_{\uparrow L_z} \tag{4.2.8}$$

To obtain relation between ↑ and ↓ coefficients it is necessary to apply lowering operator to Eq. (4.2.1) :

$$\langle J, J_Z|L_-|L, L_z\rangle \otimes |\downarrow\rangle = \langle J, J_Z|J_+^* - S_-|L, L_z\rangle \otimes |\downarrow\rangle \tag{4.2.9}$$

$$\begin{aligned}\sqrt{(L + L_z)(L - L_z + 1)}\langle J, J_Z|L, L_z - 1\rangle \otimes |\downarrow\rangle = \\ \sqrt{(J - J_Z)(J + J_Z + 1)}\langle J, J_Z + 1|L, L_z\rangle \otimes |\downarrow\rangle\end{aligned} \tag{4.2.10}$$

For $J = L + 1/2$, $J_Z + 1 = L_z - 1/2$ Eq. (4.2.10) gives:

$$A_{\downarrow L_z} = \frac{\sqrt{(L - L_z + 1)}}{\sqrt{(L - L_z)}}A_{\downarrow L_z+1} \tag{4.2.11}$$

To get relation between $A_\uparrow$ and $A_\downarrow$ the lowering operator should be applied to the state $|L, L_z\rangle \bigotimes |\uparrow\rangle$:

$$\begin{gathered}\langle J, J_Z|L_-|L, L_z\rangle \otimes |\uparrow\rangle = \\ \langle J, J_Z|J_+^* - S_-|L, L_z\rangle \otimes |\uparrow\rangle\end{gathered} \tag{4.2.12}$$

$$\begin{aligned}&\langle J, J_Z|L, L_z-1, \uparrow\rangle = \\ &\frac{\sqrt{(J-J_Z)(J+J_Z+1)}}{\sqrt{(L+L_z)(L-L_z+1)}}\langle J, J_Z+1|L, L_z, \uparrow\rangle - \\ &\frac{1}{\sqrt{(L+L_z)(L-L_z+1)}}\langle J, J_Z|L, L_z, \downarrow\rangle\end{aligned} \tag{4.2.13}$$

For $J = L + 1/2$ and $J_Z = L_z - 1/2$:

$$\begin{aligned}\langle L+\frac{1}{2}, L_z-\frac{1}{2}|L, L_z-1, \uparrow\rangle = &\frac{\sqrt{L+L_z+1}}{\sqrt{L+L_z}}\langle L+\frac{1}{2}, L_z+\frac{1}{2}|L, L_z, \uparrow\rangle - \\ &\frac{1}{\sqrt{(L+L_z)(L+L_z+1)}}\langle L+\frac{1}{2}, L_z-\frac{1}{2}|L, L_z, \downarrow\rangle\end{aligned} \tag{4.2.14}$$

$$A_{\uparrow L_z-1} = \frac{\sqrt{L+L_z+1}}{\sqrt{L+L_z}}A_{\uparrow L_z} - \frac{1}{\sqrt{(L+L_z)(L+L_z+1)}}A_{L_z\downarrow} \tag{4.2.15}$$

Using Eq. 4.2.11 Eq. (4.2.15) transforms into:

$$\frac{A_{\downarrow L_z}}{\sqrt{(L-L_z+1)}} = \frac{A_{\uparrow L_z}}{\sqrt{(L+L_z+1)}} \tag{4.2.16}$$

To get relation between $B_{\uparrow L_z}$ and $B_{\downarrow L_z}$ one should substitute $J = L - 1/2$ and $J_Z = M - 1/2$ in Eq. (4.2.13):

$$\frac{B_{\uparrow L_z}}{\sqrt{(L-L_z)}} = -\frac{B_{\downarrow L_z}}{\sqrt{(L+L_z)}} \tag{4.2.17}$$

Normalization of Eqs. (4.2.2) and (4.2.3) gives:

$$A^2_{\uparrow L_z} + B^2_{\uparrow L_z} = 1 \tag{4.2.18}$$

$$A^2_{\downarrow L_z} + B^2_{\downarrow L_z} = 1 \tag{4.2.19}$$

Using relations between $B_{\uparrow L_z}$ and $B_{\downarrow M}$, $A_{\uparrow L_z}$ and $A_{\downarrow L_z}$ Eq. (4.2.19) can be rewritten in the flowing form:

$$A^2_{\uparrow L_z} \frac{L - L_z + 1}{L + L_z + 1} + B^2_{\uparrow M} \frac{L + L_z}{L - L_z} = 1 \tag{4.2.20}$$

Solving system of equation with two unknown:

$$A^2_{\uparrow L_z} + B^2_{\uparrow L_z} = 1 \tag{4.2.21}$$

$$A^2_{\uparrow L_z} \frac{L - L_z + 1}{L + L_z + 1} + B^2_{\uparrow L_z} \frac{L + L_z}{L - L_z} = 1 \tag{4.2.22}$$

gives the flowing expressions for coefficients A and B:

$$A_{\uparrow L_z} = \frac{\sqrt{L + L_z + 1}}{\sqrt{2L + 1}} \tag{4.2.23}$$

$$B_{\uparrow L_z} = \frac{\sqrt{L - L_z}}{\sqrt{2L + 1}} \tag{4.2.24}$$

The wave function of the initial state of spin system in the extended basis of spin and macrospin, before the electron is scattered by the magnetization:

$$\begin{aligned}\Psi_i = \frac{1}{\sqrt{2L+1}}\Big(& a\sqrt{L+L_z+1}|L+\frac{1}{2},L_z+\frac{1}{2}\rangle \\ & +a\sqrt{L-L_z}|L-\frac{1}{2},L_z+\frac{1}{2}\rangle \\ & +b\sqrt{L-L_z+1}|L+\frac{1}{2},L_z-\frac{1}{2}\rangle \\ & -b\sqrt{L+L_z}|L-\frac{1}{2},L_z-\frac{1}{2}\rangle\Big)\end{aligned} \tag{4.2.25}$$

4.3 Time evolution

The spin wavefunction evolves due to the exchange interaction between the magnetization and the electron spin according to:

$$\Psi_f = U(t)\Psi_i = e^{i\frac{\hat{H}_{ex}t}{\hbar}}\Psi_i \tag{4.3.1}$$

The Zeeman contribution due to magnetic field is negligible compared to the exchange, and can be neglected in the analysis of the scattering. The components of the expanded spin basis are the eigenstates of the exchange Hamiltonian, $\hat{H}_{ex}|L \pm \frac{1}{2}, J_z\rangle = \pm E_{ex}/2$. As a result of the time evolution, the component $|L+\frac{1}{2}, L_z \pm \frac{1}{2}\rangle$ of the wavefunction accumulates a phase $\phi = E_{ex}t_f/2\hbar$ over the scattering time t_f, while the component $|L-\frac{1}{2}, L_z \pm \frac{1}{2}\rangle$ accumulates a phase $-\phi$. The final state of the spin wavefunction after scattering is:

$$\begin{aligned}\Psi_f = \frac{1}{\sqrt{2L+1}}\Big(& ae^{i\phi}\sqrt{L+L_z+1}|L+\frac{1}{2},L_z+\frac{1}{2}\rangle \\ & +ae^{-i\phi}\sqrt{L-L_z}|L-\frac{1}{2},L_z+\frac{1}{2}\rangle \\ & +be^{i\phi}\sqrt{L-L_z+1}|L+\frac{1}{2},L_z-\frac{1}{2}\rangle \\ & -be^{-i\phi}\sqrt{L+L_z}|L-\frac{1}{2},L_z-\frac{1}{2}\rangle\Big).\end{aligned} \tag{4.3.2}$$

The Clebsch–Gordan coefficients are used to express this state in terms of the direct product of the macrospin and electron spin states,

$$\begin{aligned}\Psi_f = \frac{1}{2L+1}\Big(e^{i\phi}\Big(&a\big((L+L_z+1)|L,L_z\rangle|\uparrow\rangle + (\sqrt{L+L_z+1}\sqrt{L-L_z})|L,L_z+1\rangle|\downarrow\rangle\big)\\ &+b\big((L-L_z+1)|L,L_z\rangle|\downarrow\rangle + (\sqrt{L-L_z+1}\sqrt{L+L_z})|L,L_z-1\rangle|\uparrow\rangle\big)\Big)\\ &+e^{-i\phi}\Big(a\big((L-L_z)|L,L_z\rangle|\uparrow\rangle - (\sqrt{L+L_z+1}\sqrt{L-L_z})|L,L_z+1\rangle|\downarrow\rangle\big)\\ &+b\big((L+L_z)|L,L_z\rangle|\downarrow\rangle - (\sqrt{L-L_z+1}\sqrt{L+L_z})|L,L_z-1\rangle|\uparrow\rangle\big)\Big)\Big).\end{aligned} \qquad (4.3.3)$$

The difference between expectation value of the final and the initial states gives change of spin due to scattering:

$$\Delta s_z = \langle s_z\rangle_f - \langle s_z\rangle_i = \frac{a^2((2L_z+1)^2-(2L+1)^2)}{2(2L+1)^2} + \frac{b^2((2L+1)^2-(-2L_z+1)^2)}{2(2L+1)^2}. \qquad (4.3.4)$$

This difference is equivalent to the expected change of magnon population $< \Delta N >$. For small magnon populations, when $N = L - L_x \ll L$ Eq. (4.3.4) can be simplified:

$$< \Delta N >= -\frac{a^2}{L}N + \frac{b^2}{L}N + \frac{b^2}{L}. \qquad (4.3.5)$$

The first $-\frac{a^2}{L}N$ term in the Eq. (4.3.5) describes the probability of magnon annihilation in macrospin S caused by scattering of single spin s. The second term $\frac{b^2}{L}N$, which depends on N gives a probability of stimulated magnon generation, while the third term $\frac{b^2}{L}$ does not depends on N gives probability of spontaneous magnon generation. These probabilities are equivalent to Eisensteins' coefficients, which describes the probabilities of boson generation and annihilation.

Electron current flowing through magnet can change magnon population in it. For particle current $I_p = I/e$ of electrons with polarization $p = |a|^2 - |b|^2$ scattered by the macrospin L , Eq. (4.3.5) gives the rate of variation of magnon population due to spin transfer:

$$\left.\frac{\mathrm{d}N}{\mathrm{d}t}\right|_{ST} = I_p\left(-\frac{a^2}{L}N + \frac{b^2}{L}N + \frac{b^2}{L}\right) = I_p\frac{-2pN+1-p}{2L} \qquad (4.3.6)$$

This contribution is counteracted by the relaxation, which can be described by the Landau-Gilbert damping, or equivalently by the relaxation-time approximation of the Bloch-Bloembergen theory [73, 96], $\frac{\mathrm{d}N}{\mathrm{d}t}|_R = -\frac{(N-N_0)}{\tau}$, where $N_0 = \frac{1}{\exp(\hbar\omega/k_BT)-1}$ is the magnon population in thermal equilibrium, and $\tau = \frac{1}{2\omega\alpha_G}$ is the relaxation time constant for the FMR mode. In these expressions, k_B is the Boltzmann constant, T is the temperature, ω is the FMR frequency, and α_G is the Gilbert damping constant. The magnon population in the stationary state is determined by the balance between these two contributions,

$$N = \frac{N_0 + I_p(1/p-1)/(2I_{p,c})}{1 + I_p/I_{p,c}}, \tag{4.3.7}$$

where $I_{p,c} = L/(p\tau)$ is the critical particle current for the onset of the onset of auto-oscillation. In the limiting cases of total spin polarization ($p = \pm 1$) discussed in the text, Eq. (4.3.7) gives

$$N = \frac{N_0}{1 + I/I_c} \tag{4.3.8}$$

for scattering of spin-up electrons ($p = 1$), and

$$N = \frac{N_0 + I/I_c}{1 - I/I_c} \tag{4.3.9}$$

for scattering of spin-down electrons.

To describe the effects of electrical current in FM/NM/FM magnetic nanopillars, it is necessary to i) recast the electron scattering model into the language of electrical currents applied to the nanostructure, and ii) extend the analysis of the FMR mode to the entire spectrum of the dynamical modes of the magnetic system.

The effects of reversing the current direction in FM/NM/F nanopillars must be separately analyzed in the context of the proposed scattering model, since the latter does not explicitly incorporate the spatial coordinates of the scattered electrons. Negative current is defined as $I < 0$ to represent the electron flow from the polarizer to the active magnetic layer. The magnetizations of both layers are aligned with the saturating magnetic field. Electrons become spin-polarized (with $p > 0$) in the polarizing layer, and then scattered by the active layer. The Eq. (4.3.7) need to be modified to reflect this sign convention,

$$N(I < 0) = \frac{N_0 - I(1/p - 1)/2I_c}{1 - I/I_c}. \tag{4.3.10}$$

On the other hand, $I > 0$ describes the situation when electrons first flow through the active layer and then through the polarizer, or equivalently holes are initially polarized spin-down in the polarizer, and then scattered by the free layer. From the perspective of spin dynamics, scattering of spin-down holes is equivalent to scattering of spin-down electrons, since spin-down electron / spin-down hole pair with negligible excitation energy is equivalent to the non-perturbed state of the electronic system. A modification of Eq. (4.3.7) reflecting this situation is

$$N(I > 0) = \frac{N_0 + I(1/p - 1)/I_c}{1 - I/I_c}, \tag{4.3.11}$$

where $p > 0$ is the same as in Eq. (4.3.10). The general form applicable to any sign of current is thus

$$N(I) = \frac{N_0 + |I|(1/p - 1)/I_c}{1 - I/I_c}. \tag{4.3.12}$$

To analyze the effects of spin-polarized current on the finite-wavelength dynamical modes of the nanopillar, it is necessary to show by simple scaling argument showing that Eq. (4.3.7), with appropriate values of N_0 and $I_{p,c}$, remains approximately valid for other dynamical modes. The ferromagnet was divided into n sub-volumes with characteristic dimensions $d < \lambda$, where λ is the wavelength of the dynamical mode. The magnetization within each sub-volume is approximately uniform, and therefore can be approximated by a macrospin. Thus, for finite-wavelength modes, the problem can be reduced to that of scattering of an electron by n microspins. In contrast to the FMR case discussed above, these macrospins interact not only with the electron, but also among themselves, via dipolar and exchange interactions. These interactions cannot significantly affect the outcome of scattering, as long as the associated energy is smaller than the energy $J_{ex} \sim 0.1$ eV of the exchange interaction between the electron spin and the magnetization [97]. This condition is not satisfied only for the highest-frequency dynamical modes.

By approximating the magnetic system by n weakly interacting macrospins, the analysis of spatially non-uniform dynamical modes is reduced to that for an FMR mode discussed above. In particular, the probability of electron spin-flipping due to the interaction with i-th sub-volume is inversely proportional to its total spin L/n. However, if one neglects multiple electron scattering, the probability that an electron scatters on a particular sub-volume scales inversely with $1/n$. Thus, the dependence on n cancels out from the calculation of the total number of magnons generated/annihilated per scattered electron, so that Eq. (4.3.5) and the subsequent analysis of the stationary magnon population in the FMR mode applies also to other modes, with the values of N_0 and $I_{p,c}$ determined from the frequencies of these modes.

The dynamical mode frequencies are evaluated based on the quadratic approximation quadratic magnon dispersion $\omega = \gamma B + Dk^2/\hbar$. Here, k is the wave-vector and $D = 4 \times 10^{-40}\ Jm^2$ is the exchange stiffness of Permalloy [98]. This approximation neglects the discrete lattice effects that are important for the short-wavelength modes, generally overestimating their frequencies. Also dipolar effects are neglected that are not essential for the phenomena involving the entire magnon spectrum. The allowed values of the wavevector $\vec{k}$ are calculated using the Born-von Karman boundary conditions for the magnetization [73]. To simplify the enumeration of the dynamical modes, the shape of the nanomagnet is approximated by a rectangle with the same height and total volume as the cylindrical nanopillar, $\vec{k}_{ijl} = (\frac{\pi i}{d}, \frac{\pi j}{d}, \frac{\pi l}{h})$, where $d = \sqrt{\pi}R$ is the effective lateral size ($R = 35$ nm is the radius of the nanopillar), $h = 5$ nm is the thickness of the nanomagnet, $i, j = 1...d/a$, and $l = 1..h/a$. Here, $a = 0.2$ nm is the interatomic distance for Permalloy. The total number of modes in this approximation $\approx 2.4 \times 10^6$ for the studied nanopillar, is close to its total spin $L = MV/\mu_B = 1.7 \times 10^6$, where $M = 0.8$ J/T is the magnetization of Py, V is the volume of the nanopillar, and μ_B is the Bohr magneton.

The current dependence of the total magnon population is found by adding the contributions described by Eq. (4.3.7) for each mode,

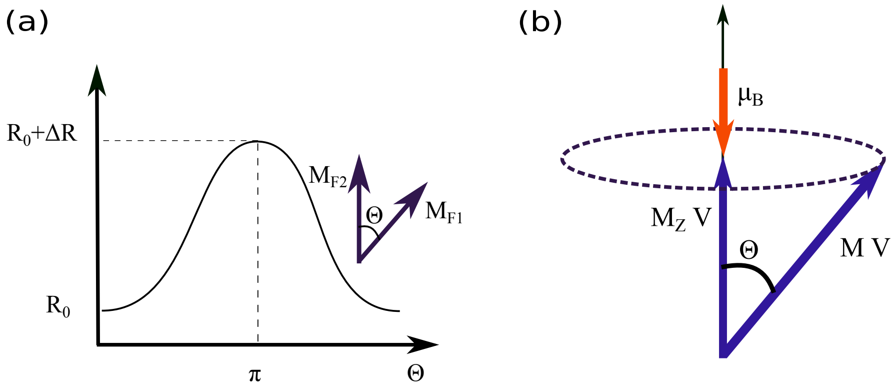

Figure 4.2: Relationship between resistance and magnon population.(a), The resistance of GMR spin valve depends on the angle between the two magnetic layers as: $R(\Theta) = R_0 + \Delta R \sin^2(\frac{\Theta}{2})$. (b), Each magnon generated decreases the effective magnetization, M_z by μ_B/V, increasing the angle Θ between M and M_z.

$$N(I) = \sum_{i=1}^{d/a}\sum_{j=1}^{d/a}\sum_{l=1}^{h/a} \frac{N_0(\omega_{ijl}) + |I|(1/p-1)/I_c(\omega_{ijl})}{1 - I/I_c(\omega_{ijl})} \tag{4.3.13}$$

with $\hbar\omega_{ijl} = \pi^2 D[\frac{i^2+j^2}{d^2} + \frac{l^2}{h}]$, $N_0(\omega_{ijl}) = \frac{1}{\exp[\hbar\omega_{ijl}]/kT-1}$, and $I_c(\omega_{ijl}) = 2\alpha\omega_{ijl}eL/(p\tau)$. To account for thermal broadening at finite temperatures, the dependence Eq. (4.3.13) was convolved with a Gaussian of width kT/R_0, where R_0 is the resistance of the nanopillar, since the thermal motion of electrons also contribute to scattering.

4.3.1 Relation between magnon population and magnetoresistance of GMR spin-valve nanopillar

Resistance of GMR spin valve depends on relative orientation of magnetization of its FM layers [Fig. 4.2(a)] and in general can be written in the following way:

$$R(\Theta) = R_0 + \Delta R \sin^2(\frac{\Theta}{2}) \tag{4.3.14}$$

where R_0 is ohmic resistance of the GMR structure ΔR – magnetoresistance and Θ – angle between magnetization orientation on FM layers.

Magnon generation increases the precession angle Θ of magnetization M around its equilibrium orientation [Fig. 4.2 (b)]. Each generated magnon reduces effective magnetization M_z, by $\mu_B V$, where μ_B is the Bohr magneton, and V is the volume of the free layer. The relation between magnon population and precession angle can be written as the following:

$$MV\cos\Theta = MV - N\mu_B \tag{4.3.15}$$

$$N = \frac{MV(1-\cos\Theta)}{\mu_B} = \frac{MV\sin^2\frac{\Theta}{2}}{\mu_B} \tag{4.3.16}$$

By combining Eq. (4.3.14) and Eq. (4.3.16) the relationship between the magnon population and the resistance of the nanopillar can be rewritten in the following form:

$$N = \frac{MV(R(\Theta) - R_0)}{2\mu_B \Delta R} \tag{4.3.17}$$

Here, one consider that magnon population is affected by spin current only “active” magnetic free layer FM1. Fluctuations in the other magnetic layer, the “polarizer” FM2, are assumed to be determined entirely by temperature T, and are accounted for by the value of ΔR in Eq. (4.3.14). One can note that the dipolar effects determined by the geometry of the ferromagnet result in variations of R on the timescale of magnetization dynamics. These effects result in a scaling correction to Eq. (4.3.17) by a factor of order 1, with the value of R representing an average over this timescale. The linear relation between N and R must hold not only for FMR, but also for other magnon modes, because their local description in terms of precession angle is the same, and GMR results from the electron scattering by the local magnetization configuration. To reinforce this argument, it is necessary consider an arbitrary spin wave mode with the largest possible mode population, describing a reversed magnetization state. In this case, Eq. (4.3.14) is clearly applicable regardless of the spatial characteristics of the mode. For smaller magnon populations, electron spin diffusion across magnetically inhomogeneous state should result in corrections to Eq. (4.3.14) of the order one. The argument presented above for a single mode also holds for the time-averaged value of R in excited states involving multiple dynamical modes, and therefore Eq. (4.3.14) applies to the total magnon population. Thus, GMR results in a linear relationship between resistance and the total magnon population in the nanomagnet are not limited to quasi-uniform modes.

4.4 Numerical calculation and results

The magnon spectrum was calculated in the approximation $\omega = \gamma B + Dk^2/\hbar$, using the lattice constant $a = 0.2$ nm and the exchange stiffness constant $D = 4 \times 10^{-40} Jm^2$ for Py [98, 99]. The allowed values of wavevector k were determined using the Born-von Karman boundary, and, to simplify mode enumeration, rectangular nanopillar shape with dimensions $63 \times 63 \times 5$ nm giving the same volume as the studied circular nanopillar with the diameter of 70 nm. The total current-dependent magnon population was calculated by adding the contributions of all the magnon modes. For each mode, the steady-state population was determined by balancing the generation rate due to ST $dN/dt|_{ST} = I[pN + signI(p+1)/2]/e$, and the relaxation $dN/dt|_r = -(N - N_0)/\tau$ [77, 92].

Figure 4.3 shows total magnon pollution calculated with Eq. (4.3.13) for different polarizations of current in the limit of $T = 0$, when thermal magnons are frozen out. When current is 100% spin polarized total number of magnons increases with increasing positive current. However, when direction of current is reversed magnon population remains constant, because there is no thermal magnons in the system and quantum fluctuation cannot be suppressed. For unpolarized current magnon are generated in both direction of current, because only electron with magnetic moment antiparallel to magnetization can generated magnon. Thereby, in a system with low population of thermal fluctuation, magnons can be generated even by unpolarized current.

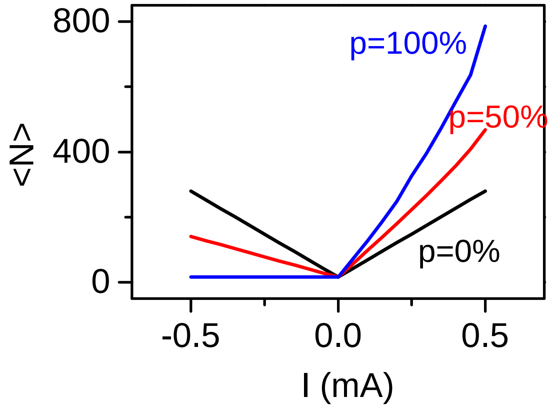

Figure 4.3: Calculated magnon population vs current for different spin polarization of current.

Chapter 5

Experimental demonstration of quantum spin transfer

5.1 Dependence of resistance of spin valve nanopillar on current at low temperatures

The effect of STT can be understood based on the argument of spin angular momentum conservation for spin-polarized electrons, scattered by a ferromagnet whose magnetization $\vec{M}$ is not aligned with the direction of polarization. The component of the electron spin transverse to $\vec{M}$ becomes absorbed, exerting a torque on the magnetization termed the spin transfer torque (STT). In nanomagnetic devices such as spin valve nanopillars [Fig. 5.2(a)], STT can enhance thermal fluctuations of magnetization, resulting in its reversal [37, 100] or auto-oscillation [38], which can be utilized in memory, microwave generation, and spin-wave logic [101, 102]. The approximation for the magnetization as a thermally fluctuating classical vector $\vec{M}$ provides an excellent description for the quasi-uniform magnetization dynamics [73]. However, the short-wavelength dynamical modes of the magnetization whose frequency extends into the THz range [73, 97] become frozen

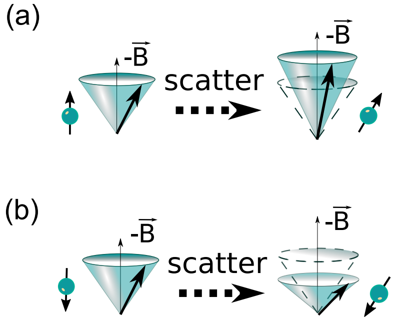

Figure 5.1: Effect of STT on thermal fluctuations. (a) Spin transfer due to scattering of the majority electrons by the magnetization results in a decrease of the thermal fluctuations. (b) Spin transfer due to scattering of the minority electrons by the magnetization results in a increase of the thermal fluctuations.

out at low temperatures.

Figure 5.1 demonstrates interaction of spin with thermal fluctuation of magnetization. Scattering of spin with anti parallel orientation to magnetic field absorbs transverse component of magnetization, exerts torque on magnetization which results in suppression of thermal fluctuations [Fig. 5.1(a)]. In contract, when spin in parallel to magnetic field B, scattering enhances thermal fluctuations [Fig. 5.1(b)]. However, in case of zero temperature, when thermal fluctuations are frozen, spin is collinear with magnetization, therefore scattering does not exert any torque.

5.2 GMR nanopillar fabrication details

Nanoscale magnetic spin-valve structure [Fig. 5.2(a)] were utilized to demonstrate that quantum zero-point fluctuations of magnetization, neglected in the existing theories of spin transfer, provide the dominant contribution to this effect at cryogenic temperatures. The demonstrated quantum spin transfer is distinguished by a non-smooth piecewise-linear dependence of the fluctuation intensity on current. The contribution of quantum spin transfer remains non-negligible even near room temperature. This effect can enhance current-induced phenomena, overcoming the efficiency limitations that are presently perceived as fundamental to the spin transfer mechanism.

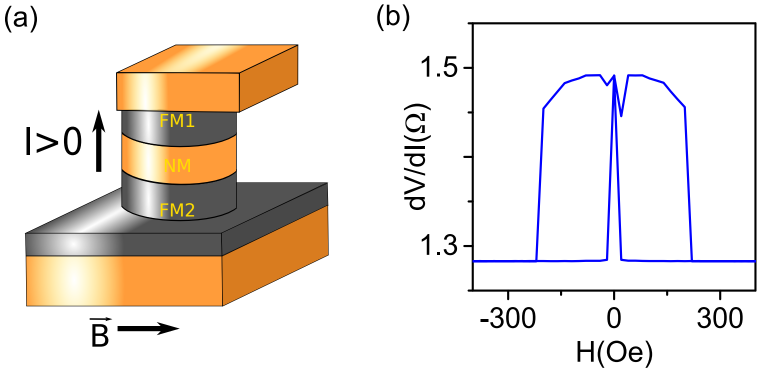

Figure 5.2: (a) Schematic of the tested spin valve. (b) Magnetoelectronic hysteresis loop.

The schematic of experimental nanodevice is show in Fig. 5.2(a). Multilayers with structure Ta(3)Cu(40)Py(10)Cu(10)Py(5)Au(5), where thicknesses are in nanometers, were deposited on Si substrates with electrodes pre-patterned by photolithography, by high-vacuum sputtering in ultrapure Argon at a base pressure of 1×10^{-8} Torr. The multilayer was removed by Ar ion milling down to the middle of Py(10) layer, everywhere except for a circular 70-nm area protected by an Al mask defined by e-beam lithography and evaporation, followed by deposition of an insulating SiO_2(15) layer without breaking vacuum. A Cu(80) top electrode was deposited, after the Al mask and the SiO_2 covering it were removed by a combination of Ar ion milling and chemical etching. Note that since the "polarizer" FM2=Py(10) was only partially patterned, magnons generated in this layer due to spin transfer can efficiently escape from the active area. Thus, spin transfer affected only the fluctuations of the free layer, while the role of was limited to polarizing the electron current flowing through the nanostructure.

5.3 Magnetoeletronic measurements

Magnetoelectronic measurements were performed in a pseudo-four probe geometry by the lock-in detection technique with an AC current of 50 μA RMS at a frequency of 1.3 kHz superimposed on the DC bias current. The magnetic field was applied in the sample plane. Its specific in-plane

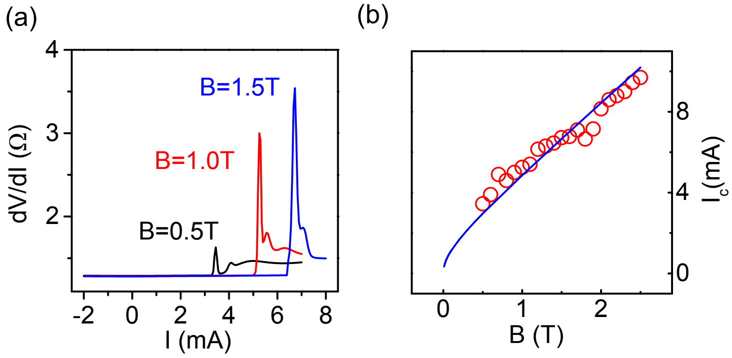

Figure 5.3: (a) Differential resistance vs current, at the label field (T=3.4 K). (b) Critical current I_C for the onset of autooscillation vs field obtained from experimental data (symbols) and the calculations (curve) obtain from Kittel formula.

direction did not affect the results. The dependence of the resistance on magnetic filed, which is shown in Fig. 5.2(b) is typical on for the GMR in magnetic magnetic nanopillars [41]. This structure shows large GMR, which is an evidence of high quality of the sample. The current dependence of differential resistance [Fig. 5.3(a)] shows a peak at positive current. This peak corresponds to onset of the dynamical instability at critical current I_C [37, 38, 67]. The value of critical current I_C increases with increasing magnetic field B [Fig. 5.3(b)] and agrees with calculation based on Kittel formula for the frequency of auto-oscillations [30].

Figure 5.4(a) shows measured differential resistance of spin valve nanopillar as a function of small applied electrical current. At subcritical currents, the resistance of the studied nanopillar exhibits an unusual piecewise-linear dependence, with a weak singularity at $I = 0$, and a slope at $I > 0$ larger than at $I < 0$. The curves are shifted by the field, which can be explained by the magnon freeze-out, as illustrated in Fig. 5.4(b) that shows the field dependence of resistance at $I = 0$, together with the calculated field-dependent thermal magnon population. The observed dependence is less abrupt, likely because the exchange approximation for magnon dispersion used in the calculation underestimates the populations of short-wavelength modes. Since the field does not noticeably affect the slopes of the curves in Fig. 5.4(a), the observed piecewise-linear dependence cannot be associated with thermal fluctuations whose intensity is controlled by the

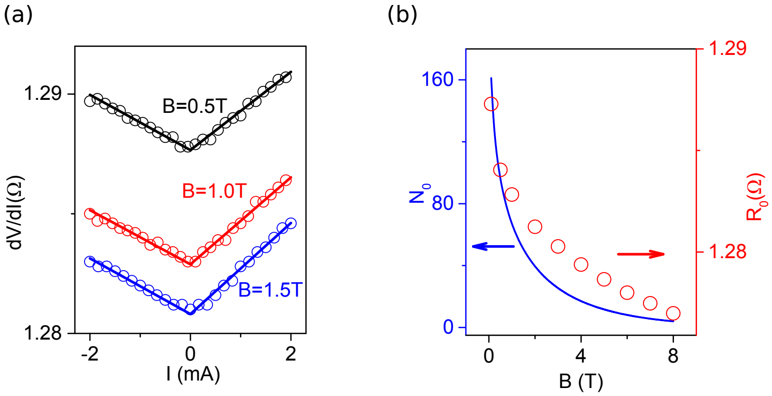

Figure 5.4: (a) Differential resistance vs current, at the label magnetic field and $T = 3.4$ K. Symbols: experimental data. Lines: best lineal fits performed for the $I < 0$ and $I > 0$ data. (b) Differential resistance (symbols, right scale) and the calculated total magnon population (curve, left scale) vs magnetic field at $I = 0$.

field [Fig. 5.4(b)]. It cannot be explained by Joule heating, because the dissipated power, and thus the resulting resistance increase, is quadratic in current [Fig. 5.5]. Electronic shot noise exhibits a similar linear increase of power with bias [103]. However, shot noise (fluctuating current) can contribute to the differential resistance only by inducing magnetization fluctuations, which in the absence of thermal fluctuations is forbidden by the angular momentum conservation argument of spin torque theory.

The previously unrecognized contribution to spin transfer, not described as enhancement of

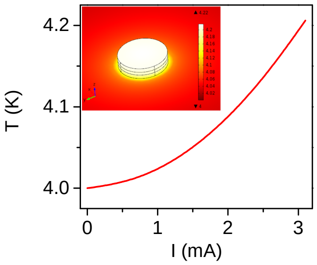

Figure 5.5: Dependence of temperature in the free layer on the electrical current applied to the nanopillar calculated with COMSOL simulation software. Inset: Temperature distribution in the nanopillar calculated at $I = 3$ mA.

Figure 5.6: (a) Scattering of majority electron by magnetization experiencing only quantum fluctuations. (b) Scattering of minority electron by magnetization enhance quantum fluctuations.

thermal magnetization fluctuations, results in a linear in current increase of magnon population. When thermal fluctuations are negligible at low temperature, the spin polarization of the scattered electrons cannot be perfectly aligned with the magnetization because of the quantum fluctuations of the latter, leading to electron spin precession that can drive spin transfer. Quantum fluctuation by their nature cannot be suppressed by majority electrons, in contrast to thermal fluctuations [Fig. 5.6(a), top]. However, they can be enhanced by scattering of the minority electrons [Fig. 5.6(c), bottom]. To satisfy angular momentum conservation, the transverse to the field components of the magnetization must remain zero.

At higher temperatures, the zero-current singularity becomes rapidly broadened [Fig. 5.7(b)]. This cannot be attributed to the increasing role of thermal magnetization fluctuations, since the piecewise-linear dependence is still apparent at larger currents even at 20 K. To analyze this effect, the data were fitted with a piecewise-linear dependence convolved with a Gaussian. The extracted broadening closely follows a linear dependence $\Delta I = (1.9 \pm 0.1)kT/eR_0$, in Fig. 5.7(a). Calculation based on the summation of Eq. (4.3.13) convolved with a Gaussian of width $1.9kT/eR_0$ [curves Fig. 5.7(b)] somewhat overestimates the classical contribution, as apparent from results for $T = 20$ K. A reasonable overall agreement with the observed temperature dependence supports the validity of the model of quantum spin transfer.

The observed thermal broadening is consistent with the proposed quantum mechanism. Bias current shifts the electron distribution in the magnetic nanopillar, driving the spin transfer [Fig. 5.7(c)]. At finite temperature, the electron distribution becomes thermally broadened, resulting in scattering of thermally excited electrons and holes [Fig. 5.7(d)] equivalent to a distribution of width

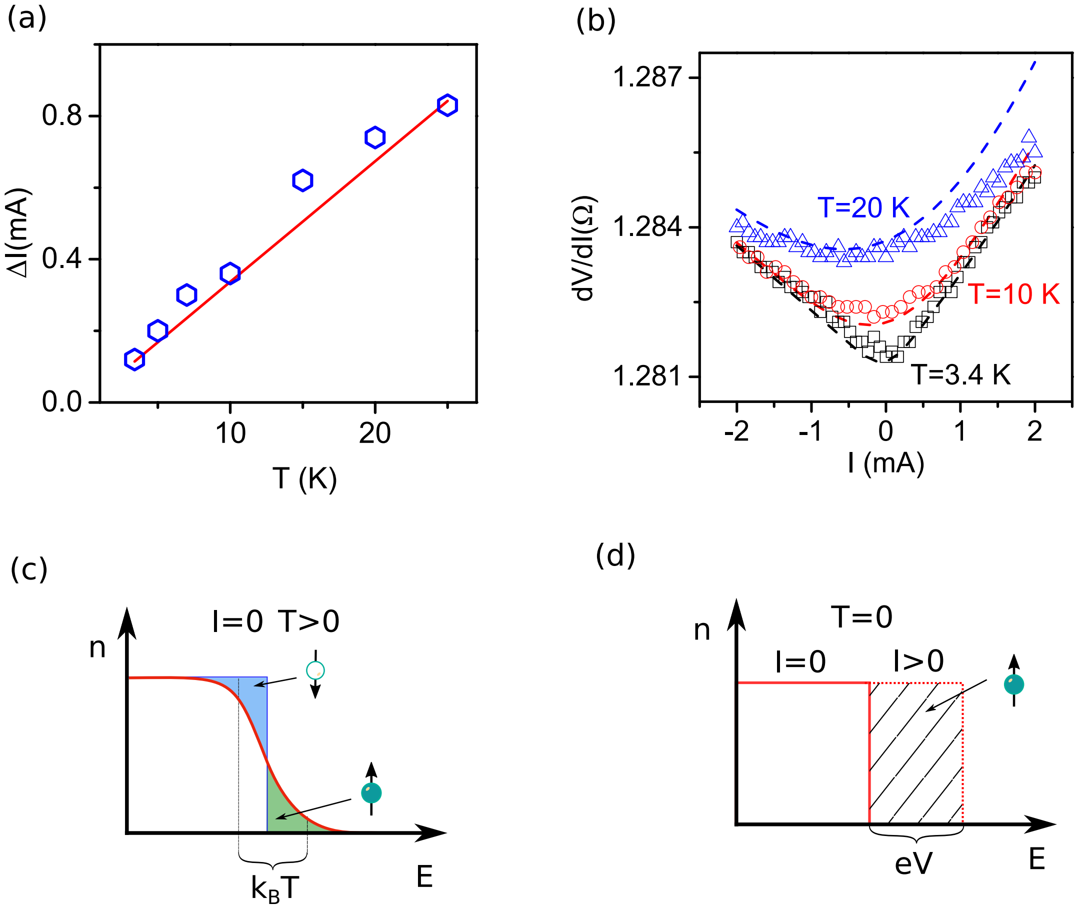

Figure 5.7: (a) Dependence of thermal broadening on temperature obtained from data by fitting the piece-wise linear dependence convolved with Gaussian (symbols), and $\Delta I = 1.9\frac{kT}{eR_0}$ (line). (b) Symbols: Differential resistance vs current at label values of temperature and magnetic field $B = 1$ T. Curves: calculation based of Eq. (4.3.13) convolved with a Gaussian of FWHM $\Delta I = 1.9\frac{kT}{eR_0}$. (c) At $T = 0$, the Fermi distribution of scattered electrons is step-like. Bias current shifts the distribution, driving the spin transfer. (d) At finite temperature $T > 0$, scattering of thermal electrons and holes occurs even at zero bias, equivalent to bias distribution of width $\frac{k_BT}{e}$.

$\Delta V = kT/e$ of the bias voltage applied to FM1, facilitating spin transfer even in the absence of directional current flow. The relation $\Delta I = (1.9 \pm 0.1)kT/eR_0$ obtained by fitting the data [Fig. 5.7(a)] is consistent with the approximately equal contributions of layers FM1 and FM2 to the total resistance R_0, such that $\Delta V \approx IR_0/2$.

Thermal broadening washes out the singular piecewise-linear dependence. However, the analysis of the dependence of magnon population around zero current at elevated temperatures demonstrates that the contribution of quantum fluctuations to spin transfer is still significant. Since the slopes of the piecewise-linear dependence are different for positive and negative currents, the value of dN/dI at $I = 0$ remains finite even in the presence of thermal broadening. By convolving the dependence $N(I)$ [Eq. (4.3.13)] for classical contribution due to thermal fluctuations with a Gaussian and differentiating with respect to I, the slope $dN/dI = N_0/I_c^{(\mathbf{i})}$ can be obtained [solid curve in Fig. 5.8(a)]. The quantum contribution, which is described by the second term in Eq. (4.3.13), has no derivative due to singularity at zero current, but by convolving it with Gaussian a smooth dependence at zero current is obtained. Differentiating the convoluted expression with respect to I gives $dN/dI = 1/2I_c^{(\mathbf{i})}$ at $I = 0$ [dashed curve in Fig. 5.8(a)], which is independent of temperature and is equivalent to the difference between the slopes at $I = +0$ and $I = -0$. The calculated classical contribution increases almost linearly with temperature (solid curve), indicating that it is dominated by the degenerately populated low-frequency modes described by the Rayleigh-Jeans law. At field $B = 1$ T, the calculated crossover from predominantly quantum to the classical spin transfer regime occurs at temperature $T_x = 38$ K. The slope $dR/dI(I = 0)$ determined from the measurements increases linearly with temperature [Fig. 5.8(b)], in agreement with the model. The $T = 0$ intercept represents the quantum contribution, and the slope reflects the classical one. Crossover temperature T_x was obtained by extrapolation of data, when value of slope dR/dI, which describes classical contribution is equal twice of intercept at $T = 0$, which describes quantum contributions. The value $T_x = 160$ K from experimental data is larger than calculated, likely because the exchange approximation for the magnon dispersion used in our calculations underestimates the quantum contribution. Based on the data in Fig. 5.8(b), estimated characteristic frequency of

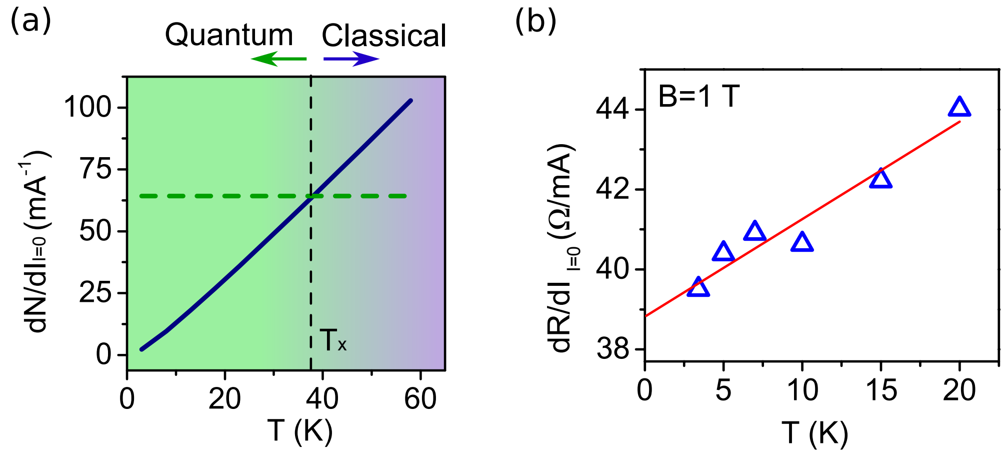

Figure 5.8: (a) The calculated slope dN/dI, at $I = 0$ and $B = 1$ T, for the classical (blue curve) and quantum (horizontal green line) contributions to the dependence of magnon population on current. T_x marks the crossover temperature between the quantum and the classical regimes. (b) Symbols: The slope dR/dI of resistance vs current at $I = 0$ and $B = 1$ T. Line: best linear fit of the data.

magnons involved in spin transfer is $f_0 = 2k_BT_x/h \approx 7$ THz, evidencing the fact that high energy modes have a significant contribution to ST.

Chapter 6

Summary

In this work, magnetization dynamics excited by spin current was studied in spintronic devices with different geometries. It has been shown that spectral, thermal and electrical properties of these devices can be modified and enhanced by optimizing the device geometry, which can become important for the future development of spintronic devices. In addition, this work demonstrated, both theoretically and experimentally, that quantum fluctuation of magnetization can provide a significant contribution to current-induced magnetization dynamics both at cryogenic and at room temperatures.

Spin Hall nanooscillators (SHNO) can generate microwave signals at cryogenic temperature. However, their operation at room temperature is poor. In my thesis research, it was demonstrated that SHNO with a nanopatterned spin injector exhibit improved efficiency and spectral characteristics. Calculations showed that the reduced size of spin injector increases the current concentration in the active area of the device, thereby reducing the total current required for the device operation. In addition, these devices exhibit narrower generation spectral lines, higher oscillation amplitudes, and can generate microwave signals in a larger range of temperatures, extending to room temperature.

It was also shown that the spectral characteristics of SHNO devices can be improved by using non-uniform fields arising due to the demagnetizing effects in nanopatterned ferromagnets. SHNO devices based on a bow-tie-shaped nanocostriction, formed both in the spin Hall layer and in the active ferromagnetic layer, are characterized by efficient current concentration, enabling the generation of coherent oscillation at smaller driving currents. The combined effects of the demagnetizing and Oersted fields result in spin waves localization in active area, increased amplitude of oscillation, and higher generated microwave power. The demonstrated nanoconstriction SHNO device is characterized by a relatively large oscillation volume, resulting in improved coherence of auto-oscillations.

In addition to improved characteristics of SHNO devices, it was demonstrated that spin-Hall nano-oscillators can be efficiently synchronized to external microwave signals, providing a route for the optimization of high-frequency spintronic devices for future-generation microelectronic circuits. Since the geometry of SHNO facilitates direct optical access to the active device area, they also present an unprecedented opportunity for the fundamental studies of nonlinear dynamic phenomena in nanoscale systems. Additionally, the results elucidate the general effects of thermal noise on the synchronization characteristics of STNOs, which may explain some of the recent observations in structures based on magnetic tunnel junctions.

The demonstrated quantum contributions to current induced phenomena can be particularly important for the future development of efficient spintronic devices. Quantum fluctuations can contribute to current-induced phenomena whenever highly nonuniform dynamical states are involved, for example in reversal via domain wall motion in technologically important nanomagnets with perpendicular magnetic anisotropy [82]. More generally, the demonstrated magnon generation mechanism can decrease the effective magnetization, lowering the reversal barriers. The effects of quantum fluctuations on spin transfer in antiferromagnets [104] are likely larger than in ferromagnets, due to much higher magnon frequencies. Quantum fluctuations may contribute to other phenomena involving interaction between magnetization and conduction electrons, including spin pumping [105], spin-orbit effects [64, 106, 107], optically-driven effects [108–110], and spin-caloric effects [111–115].

Based on the demonstrated quantum effects, one can also infer a significant inelastic contribution to spin-dependent electron transport in ferromagnets due to quantum electron-magnon scattering. Specifically, it is presently believed that currents flowing through ferromagnets become spin-polarized mainly due to spin-anisotropy of electron scattering. Meanwhile, according to Eq. (4.3.13), an unpolarized conduction electron scattered by the ferromagnet generates a magnon in a given dynamical mode with probability $1/2S$, where S is the total spin of the ferromagnet; it becomes majority spin-polarized in this process. The number of modes is of order S [73], and therefore the total probability for an initially unpolarized electron to become majority-polarized due to quantum magnon generation is of order 1. This result shows that inelastic scattering of electrons by quantum magnetization fluctuations provides a non-negligible contribution to spin-polarizing properties of ferromagnets.

Bibliography

[1] Y. K. Kato, "Observation of the spin hall effect in semiconductors," *Science*, vol. 306, pp. 1910–1913, dec 2004.

[2] Stanford Research Systems,, *About Lock-In Amplifiers,*. Also available as http://www.thinksrs.com/support/app.htm.

[3] A. Yoshihara, H. Sato, and J.-i. Mawatari, "Brillouin light scattering from spin waves in Co\ V Cr V alloy" lms," *Journal of Magnetism and . . .* , vol. 221, pp. 261–267, 2000.

[4] S. Demokritov and V. Demidov, "Micro-Brillouin light scattering spectroscopy of magnetic nanostructures," *Magnetics, IEEE Transactions on*, vol. 44, no. 1, pp. 6–12, 2008.

[5] V. E. Demidov, S. Urazhdin, H. Ulrichs, V. Tiberkevich, A. Slavin, D. Baither, G. Schmitz, and S. O. Demokritov, "Magnetic nano-oscillator driven by pure spin current," *Nature Materials*, oct 2012.

[6] A. Hoffmann, "Viewpoint: Make your spins spin."

[7] A. Zholud and S. Urazhdin, "Microwave generation by spin hall nanooscillators with nanopatterned spin injector," *Applied Physics Letters*, vol. 105, p. 112404, sep 2014.

[8] V. E. Demidov, S. Urazhdin, A. Zholud, A. V. Sadovnikov, and S. O. Demokritov, "Nanoconstriction-based spin-hall nano-oscillator," *Applied Physics Letters*, vol. 105, p. 172410, oct 2014.

[9] V. E. Demidov, H. Ulrichs, S. V. Gurevich, S. O. Demokritov, V. S. Tiberkevich, A. N. Slavin, A. Zholud, and S. Urazhdin, “Synchronization of spin hall nano-oscillators to external microwave signals,” *Nature Communications*, vol. 5, jan 2014.

[10] I. L. Markov, “Limits on fundamental limits to computation,” *Nature*, vol. 512, pp. 147–154, aug 2014.

[11] R. Keyes, “Fundamental limits of silicon technology,” *Proceedings of the IEEE*, vol. 89, pp. 227–239, mar 2001.

[12] R. Zia, J. A. Schuller, A. Chandran, and M. L. Brongersma, “Plasmonics: the next chip-scale technology,” *Materials Today*, vol. 9, pp. 20–27, jul 2006.

[13] M. I. Stockman, “Nanoplasmonics: past, present, and glimpse into future,” *Optics Express*, vol. 19, p. 22029, oct 2011.

[14] S. A. Wolf, D. D. Awschalom, R. A. Buhrman, J. M. Daughton, S. von Molnár, M. L. Roukes, A. Y. Chtchelkanova, and D. M. Treger, “Spintronics: A spin-based electronics vision for the future,” *Science*, vol. 294, no. 5546, pp. 1488–1495, 2001.

[15] N. Locatelli, V. Cros, and J. Grollier, “Spin-torque building blocks,” *Nature Materials*, vol. 13, pp. 11–20, dec 2013.

[16] A. Fert, “The present and the future of spintronics,” *Thin Solid Films*, vol. 517, no. 1, pp. 2 – 5, 2008. Fifth International Conference on Silicon Epitaxy and Heterostructures (ICSI-5).

[17] S. Parkin and S.-H. Yang, “Memory on the racetrack,” *Nature Nanotechnology*, vol. 10, pp. 195–198, mar 2015.

[18] K. Ando, S. Fujita, J. Ito, S. Yuasa, Y. Suzuki, Y. Nakatani, T. Miyazaki, and H. Yoda, “Spin-transfer torque magnetoresistive random-access memory technologies for normally off computing (invited),” *Journal of Applied Physics*, vol. 115, no. 17, p. 172607, 2014.

[19] Z. An, F. Q. Liu, Y. Lin, and C. Liu, "The universal definition of spin current," *Scientific Reports*, vol. 2, may 2012.

[20] G. A. Prinz, "Magnetoelectronics," *Science*, vol. 282, pp. 1660–1663, nov 1998.

[21] V. V. Kruglyak, S. O. Demokritov, and D. Grundler, "Magnonics," *Journal of Physics D: Applied Physics*, vol. 43, p. 264001, jun 2010.

[22] A. V. Chumak, V. I. Vasyuchka, A. A. Serga, and B. Hillebrands, "Magnon spintronics," *Nature Physics*, vol. 11, pp. 453–461, jun 2015.

[23] J. Shi, P. Zhang, D. Xiao, and Q. Niu, "Proper definition of spin current in spin-orbit coupled systems," *Phys. Rev. Lett.*, vol. 96, p. 076604, Feb 2006.

[24] Q.-f. Sun and X. C. Xie, "Definition of the spin current: The angular spin current and its physical consequences," *Phys. Rev. B*, vol. 72, p. 245305, Dec 2005.

[25] D. Culcer, J. Sinova, N. A. Sinitsyn, T. Jungwirth, A. H. MacDonald, and Q. Niu, "Semiclassical spin transport in spin-orbit-coupled bands," *Phys. Rev. Lett.*, vol. 93, p. 046602, Jul 2004.

[26] X. Zhou, Z. Zhang, and C.-Z. Hu, "Spin continuity equation and definition of spin current," 2009.

[27] D. J. Griffiths, *Introduction to Quantum Mechanics (2nd Edition)*. Pearson Prentice Hall, 2004.

[28] Anonymous, "Abstracts of papers to be presented at the 1955 thanksgiving meeting at the university of chicago, chicago, illinois, november 25 and 26, 1955," *Phys. Rev.*, vol. 100, pp. 1235–1235, Nov 1955.

[29] M. C. Hickey and J. S. Moodera, "Origin of intrinsic gilbert damping," *Physical Review Letters*, vol. 102, mar 2009.

[30] C. Kittel, "On the theory of ferromagnetic resonance absorption," *Phys. Rev.*, vol. 73, pp. 155–161, Jan 1948.

[31] M. Dyakonov and V. Perel, "Current-induced spin orientation of electrons in semiconductors," *Physics Letters A*, vol. 35, pp. 459–460, jul 1971.

[32] M. I. Dyakonov and V. I. Perel, "Possibility of orientating electron spins with current," *Sov. Phys. JETP Lett.*, vol. 13, 1971.

[33] T. Yang, T. Kimura, and Y. Otani, "Giant spin-accumulation signal and pure spin-current-induced reversible magnetization switching," *Nature Physics*, vol. 4, pp. 851–854, oct 2008.

[34] Y. Kajiwara, K. Harii, S. Takahashi, J. Ohe, K. Uchida, M. Mizuguchi, H. Umezawa, H. Kawai, K. Ando, K. Takanashi, S. Maekawa, and E. Saitoh, "Transmission of electrical signals by spin-wave interconversion in a magnetic insulator," *Nature*, vol. 464, pp. 262–266, mar 2010.

[35] L. Liu, C.-F. Pai, Y. Li, H. W. Tseng, D. C. Ralph, and R. A. Buhrman, "Spin-torque switching with the giant spin hall effect of tantalum," *Science*, vol. 336, pp. 555–558, may 2012.

[36] J. Slonczewski, "Current-driven excitation of magnetic multilayers," *J. Magn. Magn. Mater.*, vol. 159, pp. L1–L7, jun 1996.

[37] J. A. Katine, F. J. Albert, R. A. Buhrman, E. B. Myers, and D. C. Ralph, "Current-driven magnetization reversal and spin-wave excitations in co /cu /co pillars," *Phys. Rev. Lett.*, vol. 84, pp. 3149–3152, Apr 2000.

[38] S. I. Kiselev, J. C. Sankey, I. N. Krivorotov, N. C. Emley, R. J. Schoelkopf, R. A. Buhrman, and D. C. Ralph, "Microwave oscillations of a nanomagnet driven by a spin-polarized current," *Nature*, vol. 425, pp. 380–383, Sep 2003.

[39] W. H. Rippard, M. R. Pufall, S. Kaka, S. E. Russek, and T. J. Silva, "Direct-current induced dynamics in $\mathrm{co}_{90}\mathrm{fe}_{10}/\mathrm{ni}_{80}\mathrm{fe}_{20}$ point contacts," *Phys. Rev. Lett.*, vol. 92, p. 027201, Jan 2004.

[40] G. Binasch, P. Grünberg, F. Saurenbach, and W. Zinn, "Enhanced magnetoresistance in layered magnetic structures with antiferromagnetic interlayer exchange," *Phys. Rev. B*, vol. 39, pp. 4828–4830, Mar 1989.

[41] M. N. Baibich, J. M. Broto, A. Fert, F. N. Van Dau, F. Petroff, P. Etienne, G. Creuzet, A. Friederich, and J. Chazelas, "Giant magnetoresistance of (001)fe/(001)cr magnetic superlattices," *Phys. Rev. Lett.*, vol. 61, pp. 2472–2475, Nov 1988.

[42] D. Ralph and M. Stiles, "Spin transfer torques," *Journal of Magnetism and Magnetic Materials*, vol. 320, pp. 1190–1216, apr 2008.

[43] T. McGuire and R. Potter, "Anisotropic magnetoresistance in ferromagnetic 3d alloys," *IEEE Transactions on Magnetics*, vol. 11, pp. 1018–1038, jul 1975.

[44] J. Bass and W. Pratt, "Current-perpendicular (CPP) magnetoresistance in magnetic metallic multilayers," *Journal of Magnetism and Magnetic Materials*, vol. 200, pp. 274–289, oct 1999.

[45] L. Brillouin, "Diffusion of light and X-ray by a transparent homogeneous body. The influence of thermal agitation," *Annales de Physique(Paris)*, no. 17, pp. 88–122, 1922.

[46] M. Cardona and G. Guntherodt, "Light scattering in solids viii - fullerenes, semiconductor surfaces, coherent phonons - introduction," *Light Scattering in Solids Viii*, vol. 76, pp. 1–26, 2000.

[47] S. H. Kong, M. V. Klein, F. Tsui, and C. P. Flynn, "Brillouin-light-scattering study of long-wavelength acoustic phonons in single-crystal dysprosium films," *Phys. Rev. B*, vol. 50, pp. 18497–18504, Dec 1994.

[48] S. O. Demokritov, B. Hillebrands, and A. N. Slavin, "Brillouin light scattering studies of confined spin waves: linear and nonlinear confinement," *Physics Reports*, vol. 348, pp. 441–489, 2001.

[49] M. Buchmeier, H. Dassow, D. E. Bürgler, and C. M. Schneider, “Intensity of Brillouin light scattering from spin waves in magnetic multilayers with noncollinear spin configurations: Theory and experiment,” *Physical Review B*, vol. 75, no. 18, p. 19, 2007.

[50] R. W. Boyd, *Nonlinear optics.* Amsterdam ; Boston: Academic Press, 3rd ed., 2008.

[51] C. W. Sandweg, M. B. Jungfleisch, V. I. Vasyuchka, a. a. Serga, P. Clausen, H. Schultheiss, B. Hillebrands, a. Kreisel, and P. Kopietz, “Wide-range wavevector selectivity of magnon gases in Brillouin light scattering spectroscopy.,” *The Review of scientific instruments*, vol. 81, p. 073902, July 2010.

[52] V. E. Demidov, S. O. Demokritov, B. Hillebrands, M. Laufenberg, and P. P. Freitas, “Radiation of spin waves by a single micrometer-sized magnetic element,” *Applied Physics Letters*, vol. 85, no. 14, p. 2866, 2004.

[53] R. H. Liu, W. L. Lim, and S. Urazhdin, “Spectral characteristics of the microwave emission by the spin hall nano-oscillator,” *Phys. Rev. Lett.*, vol. 110, p. 147601, Apr 2013.

[54] A. Slavin and V. Tiberkevich, “Spin wave mode excited by spin-polarized current in a magnetic nanocontact is a standing self-localized wave bullet,” *Phys. Rev. Lett.*, vol. 95, p. 237201, Nov 2005.

[55] V. E. Demidov, S. Urazhdin, and S. O. Demokritov, “Direct observation and mapping of spin waves emitted by spin-torque nano-oscillators,” *Nature Materials*, vol. 9, pp. 984–988, oct 2010.

[56] L. Liu, R. A. Buhrman, and D. C. Ralph, “Review and analysis of measurements of the spin hall effect in platinum,” 2011.

[57] S. Mizukami, Y. Ando, and T. Miyazaki, “Effect of spin diffusion on gilbert damping for a very thin permalloy layer in cu/permalloy/cu/pt films,” *Phys. Rev. B*, vol. 66, p. 104413, Sep 2002.

[58] V. E. Demidov, S. Urazhdin, E. R. J. Edwards, M. D. Stiles, R. D. McMichael, and S. O. Demokritov, "Control of magnetic fluctuations by spin current," *Phys. Rev. Lett.*, vol. 107, p. 107204, Sep 2011.

[59] W. L. Lim, N. Ebrahim-Zadeh, J. C. Owens, H. G. E. Hentschel, and S. Urazhdin, "Temperature-dependent proximity magnetism in pt," *Applied Physics Letters*, vol. 102, p. 162404, apr 2013.

[60] H. Ulrichs, V. E. Demidov, and S. O. Demokritov, "Micromagnetic study of auto-oscillation modes in spin-hall nano-oscillators," *Applied Physics Letters*, vol. 104, p. 042407, jan 2014.

[61] M. J. Donahue and D. G. Porter, *OOMMF User's Guide, Version 1.0, Interagency Report NISTIR 6376.*

[62] A. Brataas, A. D. Kent, and H. Ohno, "Current-induced torques in magnetic materials," *Nature Materials*, vol. 11, pp. 372–381, apr 2012.

[63] T. Jungwirth, J. Wunderlich, and K. Olejník, "Spin hall effect devices," *Nature Materials*, vol. 11, pp. 382–390, apr 2012.

[64] K. Ando, S. Takahashi, K. Harii, K. Sasage, J. Ieda, S. Maekawa, and E. Saitoh, "Electric manipulation of spin relaxation using the spin hall effect," *Physical Review Letters*, vol. 101, jul 2008.

[65] Z. Wang, Y. Sun, M. Wu, V. Tiberkevich, and A. Slavin, "Control of spin waves in a thin film ferromagnetic insulator through interfacial spin scattering," *Physical Review Letters*, vol. 107, sep 2011.

[66] I. M. Miron, K. Garello, G. Gaudin, P.-J. Zermatten, M. V. Costache, S. Auffret, S. Bandiera, B. Rodmacq, A. Schuhl, and P. Gambardella, "Perpendicular switching of a single ferromagnetic layer induced by in-plane current injection," *Nature*, vol. 476, pp. 189–193, jul 2011.

[67] W. H. Rippard, M. R. Pufall, S. Kaka, T. J. Silva, S. E. Russek, and J. A. Katine, “Injection locking and phase control of spin transfer nano-oscillators,” *Physical Review Letters*, vol. 95, aug 2005.

[68] B. Georges, J. Grollier, M. Darques, V. Cros, C. Deranlot, B. Marcilhac, G. Faini, and A. Fert, “Coupling efficiency for phase locking of a spin transfer nano-oscillator to a microwave current,” *Physical Review Letters*, vol. 101, jul 2008.

[69] S. Urazhdin, P. Tabor, V. Tiberkevich, and A. Slavin, “Fractional synchronization of spin-torque nano-oscillators,” *Physical Review Letters*, vol. 105, aug 2010.

[70] S. Urazhdin, V. Tiberkevich, and A. Slavin, “Parametric excitation of a magnetic nanocontact by a microwave field,” *Physical Review Letters*, vol. 105, dec 2010.

[71] J. E. Hirsch, “Spin hall effect,” *Physical Review Letters*, vol. 83, pp. 1834–1837, aug 1999.

[72] P. W. Anderson and H. Suhl, “Instability in the motion of ferromagnets at high microwave power levels,” *Physical Review*, vol. 100, pp. 1788–1789, dec 1955.

[73] A. G. Gurevich and G. A. Melkov, *Magnetization Oscillations and Waves.* CRC Press, 1996.

[74] A. Slavin and V. Tiberkevich, “Nonlinear auto-oscillator theory of microwave generation by spin-polarized current,” *IEEE Transactions on Magnetics*, vol. 45, pp. 1875–1918, apr 2009.

[75] R. W. Boyd, S. G. Lukishova, and Y. Shen, eds., *Self-focusing: Past and Present.* Springer New York, 2009.

[76] H. Risken, *The Fokker-Planck Equation.* Springer Berlin Heidelberg, 1989.

[77] L. Berger, “Emission of spin waves by a magnetic multilayer traversed by a current,” *Physical Review B*, vol. 54, pp. 9353–9358, oct 1996.

[78] M. Tsoi, A. G. M. Jansen, J. Bass, W.-C. Chiang, V. Tsoi, and P. Wyder, “Generation and detection of phase-coherent current-driven magnons in magnetic multilayers,” *Nature*, vol. 406, pp. 46–48, jul 2000.

[79] Y. B. Bazaliy, B. A. Jones, and S.-C. Zhang, “Modification of the landau-lifshitz equation in the presence of a spin-polarized current in colossal- and giant-magnetoresistive materials,” *Phys. Rev. B*, vol. 57, pp. R3213–R3216, Feb 1998.

[80] K.-J. Lee, A. Deac, O. Redon, J.-P. Nozières, and B. Dieny, “Excitations of incoherent spin-waves due to spin-transfer torque,” *Nature Materials*, vol. 3, pp. 877–881, nov 2004.

[81] A. A. Tulapurkar, Y. Suzuki, A. Fukushima, H. Kubota, H. Maehara, K. Tsunekawa, D. D. Djayaprawira, N. Watanabe, and S. Yuasa, “Spin-torque diode effect in magnetic tunnel junctions,” *Nature*, vol. 438, pp. 339–342, nov 2005.

[82] S. Mangin, D. Ravelosona, J. A. Katine, M. J. Carey, B. D. Terris, and E. E. Fullerton, “Current-induced magnetization reversal in nanopillars with perpendicular anisotropy,” *Nature Materials*, vol. 5, pp. 210–215, feb 2006.

[83] M. Madami, S. Bonetti, G. Consolo, S. Tacchi, G. Carlotti, G. Gubbiotti, F. B. Mancoff, M. A. Yar, and J. Åkerman, “Direct observation of a propagating spin wave induced by spin-transfer torque,” *Nature Nanotechnology*, vol. 6, pp. 635–638, aug 2011.

[84] K.-S. Ryu, L. Thomas, S.-H. Yang, and S. Parkin, “Chiral spin torque at magnetic domain walls,” *Nature Nanotechnology*, vol. 8, pp. 527–533, jun 2013.

[85] A. D. Kent and D. C. Worledge, “A new spin on magnetic memories,” *Nat Nano*, vol. 10, pp. 187–191, Mar 2015. Commentary.

[86] D. V. Berkov and N. L. Gorn, “Micromagnetic simulations of the magnetization precession induced by a spin-polarized current in a point-contact geometry (invited),” *Journal of Applied Physics*, vol. 99, p. 08Q701, apr 2006.

[87] S. Urazhdin, N. O. Birge, W. P. Pratt, and J. Bass, “Current-driven magnetic excitations in permalloy-based multilayer nanopillars,” *Physical Review Letters*, vol. 91, oct 2003.

[88] Y. Acremann, J. P. Strachan, V. Chembrolu, S. D. Andrews, T. Tyliszczak, J. A. Katine, M. J. Carey, B. M. Clemens, H. C. Siegmann, and J. Stöhr, “Time-resolved imaging of spin

transfer switching: Beyond the macrospin concept," *Physical Review Letters*, vol. 96, may 2006.

[89] J. P. Strachan, V. Chembrolu, Y. Acremann, X. W. Yu, A. A. Tulapurkar, T. Tyliszczak, J. A. Katine, M. J. Carey, M. R. Scheinfein, H. C. Siegmann, and J. Stöhr, "Direct observation of spin-torque driven magnetization reversal through nonuniform modes," *Physical Review Letters*, vol. 100, jun 2008.

[90] S. Bonetti, V. Tiberkevich, G. Consolo, G. Finocchio, P. Muduli, F. Mancoff, A. Slavin, and J. Åkerman, "Experimental evidence of self-localized and propagating spin wave modes in obliquely magnetized current-driven nanocontacts," *Physical Review Letters*, vol. 105, nov 2010.

[91] B. Fain and P. W. Milonni, "Classical stimulated emission," *Journal of the Optical Society of America B*, vol. 4, p. 78, jan 1987.

[92] S. Urazhdin, "Current-driven magnetization dynamics in magnetic multilayers," *Phys. Rev. B*, vol. 69, p. 134430, Apr 2004.

[93] A. Brataas, Y. V. Nazarov, and G. E. W. Bauer, "Finite-element theory of transport in ferromagnet–normal metal systems," *Physical Review Letters*, vol. 84, pp. 2481–2484, mar 2000.

[94] T. Valet and A. Fert, "Theory of the perpendicular magnetoresistance in magnetic multilayers," *Phys. Rev. B*, vol. 48, pp. 7099–7113, Sep 1993.

[95] Y. Wang and L. J. Sham, "Quantum dynamics of a nanomagnet driven by spin-polarized current," *Phys. Rev. B*, vol. 85, p. 092403, Mar 2012.

[96] V. Kambersky and C. E. Patton, "Spin-wave relaxation and phenomenological damping in ferromagnetic resonance," *Phys. Rev. B*, vol. 11, pp. 2668–2672, Apr 1975.

[97] R. M. White, *Quantum Theory of Magnetism.* Springer Berlin Heidelberg, 2007.

[98] F. Menzinger, G. Caglioti, G. Shirane, R. Nathans, S. J. Pickart, and H. A. Alperin, "Spin-wave dispersion relation in fe-ni alloys," *J. Appl. Phys.*, vol. 39, no. 2, pp. 455–457, 1968.

[99] R. N. Sinclair and B. N. Brockhouse, "Dispersion relation for spin waves in a fcc cobalt alloy," *Phys. Rev.*, vol. 120, pp. 1638–1640, Dec 1960.

[100] S. Zhang, P. M. Levy, and A. Fert, "Mechanisms of spin-polarized current-driven magnetization switching," *Physical Review Letters*, vol. 88, may 2002.

[101] B. Behin-Aein, D. Datta, S. Salahuddin, and S. Datta, "Proposal for an all-spin logic device with built-in memory," *Nature Nanotechnology*, vol. 5, pp. 266–270, feb 2010.

[102] S. S. P. Parkin, M. Hayashi, and L. Thomas, "Magnetic domain-wall racetrack memory," *Science*, vol. 320, no. 5873, pp. 190–194, 2008.

[103] L. Spietz, K. W. Lehnert, I. Siddiqi, and R. J. Schoelkopf, "Primary electronic thermometry using the shot noise of a tunnel junction," *Science*, vol. 300, no. 5627, pp. 1929–1932, 2003.

[104] T. Jungwirth, X. Marti, P. Wadley, and J. Wunderlich, "Antiferromagnetic spintronics," *Nature Nanotechnology*, vol. 11, pp. 231–241, mar 2016.

[105] Y. Tserkovnyak, A. Brataas, and G. E. W. Bauer, "Enhanced gilbert damping in thin ferromagnetic films," *Phys. Rev. Lett.*, vol. 88, p. 117601, Feb 2002.

[106] L. Liu, C.-F. Pai, Y. Li, H. W. Tseng, D. C. Ralph, and R. A. Buhrman, "Spin-torque switching with the giant spin hall effect of tantalum," *Science*, vol. 336, no. 6081, pp. 555–558, 2012.

[107] H. Nakayama, M. Althammer, Y.-T. Chen, K. Uchida, Y. Kajiwara, D. Kikuchi, T. Ohtani, S. Geprägs, M. Opel, S. Takahashi, R. Gross, G. E. W. Bauer, S. T. B. Goennenwein, and E. Saitoh, "Spin hall magnetoresistance induced by a nonequilibrium proximity effect," *Physical Review Letters*, vol. 110, may 2013.

[108] E. Turgut, D. Zusin, D. Legut, K. Carva, R. Knut, J. M. Shaw, C. Chen, Z. Tao, H. T. Nembach, T. J. Silva, S. Mathias, M. Aeschlimann, P. M. Oppeneer, H. C. Kapteyn, M. M. Murnane, and P. Grychtol, "Stoner versus heisenberg: Ultrafast exchange reduction and magnon generation during laser-induced demagnetization," *Phys. Rev. B*, vol. 94, p. 220408, Dec 2016.

[109] I. Razdolski, A. Alekhin, N. Ilin, J. P. Meyburg, V. Roddatis, D. Diesing, U. Bovensiepen, and A. Melnikov, "Nanoscale interface confinement of ultrafast spin transfer torque driving non-uniform spin dynamics," *Nature Communications*, vol. 8, Apr 2017.

[110] D. Rudolf, C. La-O-Vorakiat, M. Battiato, R. Adam, J. M. Shaw, E. Turgut, P. Maldonado, S. Mathias, P. Grychtol, H. T. Nembach, T. J. Silva, M. Aeschlimann, H. C. Kapteyn, M. M. Murnane, C. M. Schneider, and P. M. Oppeneer, "Ultrafast magnetization enhancement in metallic multilayers driven by superdiffusive spin current," *Nature Communications*, vol. 3, Sept 2012.

[111] M. Hatami, G. E. W. Bauer, Q. Zhang, and P. J. Kelly, "Thermal spin-transfer torque in magnetoelectronic devices," *Phys. Rev. Lett.*, vol. 99, p. 066603, Aug 2007.

[112] J. Foros, A. Brataas, Y. Tserkovnyak, and G. E. W. Bauer, "Magnetization noise in magnetoelectronic nanostructures," *Phys. Rev. Lett.*, vol. 95, p. 016601, Jun 2005.

[113] J.-E. Wegrowe, "Spin transfer from the point of view of the ferromagnetic degrees of freedom," *Solid State Communications*, vol. 150, pp. 519–523, mar 2010.

[114] Z. Zhang, L. Bai, X. Chen, H. Guo, X. L. Fan, D. S. Xue, D. Houssameddine, and C.-M. Hu, "Observation of thermal spin-transfer torque via ferromagnetic resonance in magnetic tunnel junctions," *Phys. Rev. B*, vol. 94, p. 064414, Aug 2016.

[115] G.-M. Choi, C.-H. Moon, B.-C. Min, K.-J. Lee, and D. G. Cahill, "Thermal spin-transfer torque driven by the spin-dependent seebeck effect in metallic spin-valves," *Nature Physics*, vol. 11, July 2015.